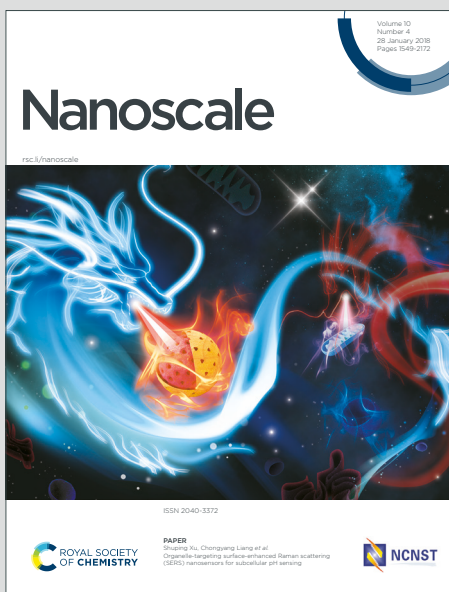


# Nanoscale

## Accepted Manuscript

This article can be cited before page numbers have been issued, to do this please use: A. C. Velazquez-Albino, B. Elsea, A. Melnyk, N. Eswaran, E. D. Imhoff, A. G. Williams, W. Graham, J. A. Johnson, C. Johnson, M. Butala and C. Rinaldi-Ramos, *Nanoscale*, 2026, DOI: 10.1039/D5NR03157E.



This is an Accepted Manuscript, which has been through the Royal Society of Chemistry peer review process and has been accepted for publication.

Accepted Manuscripts are published online shortly after acceptance, before technical editing, formatting and proof reading. Using this free service, authors can make their results available to the community, in citable form, before we publish the edited article. We will replace this Accepted Manuscript with the edited and formatted Advance Article as soon as it is available.

You can find more information about Accepted Manuscripts in the [Information for Authors](#).

Please note that technical editing may introduce minor changes to the text and/or graphics, which may alter content. The journal's standard [Terms & Conditions](#) and the [Ethical guidelines](#) still apply. In no event shall the Royal Society of Chemistry be held responsible for any errors or omissions in this Accepted Manuscript or any consequences arising from the use of any information it contains.

1 **Esterification synthesis of iron oxide nanoparticle tracers for magnetic particle imaging (MPI)**2 Ambar C. Velazquez-Albino<sup>1</sup>, Bianca Elsea<sup>1</sup>, Andrii Melnyk<sup>1</sup>, Neel Eswaran<sup>2</sup>, Eric D. Imhoff<sup>1</sup>,  
3 Aleia G. Williams<sup>3</sup>, Willem Graham,<sup>3</sup> Jacqueline Anne Johnson<sup>3</sup>, Charles E. Johnson<sup>3</sup>, Megan  
4 M. Butala<sup>2</sup>, and Carlos M. Rinaldi-Ramos<sup>1,4,\*</sup>5 <sup>1</sup>Department of Chemical Engineering, University of Florida, Gainesville, FL 32611, USA6 <sup>2</sup>Department of Materials Science and Engineering, University of Florida, Gainesville, FL  
7 32611, USA8 <sup>3</sup>Department of Mechanical, Aerospace and Biomedical Engineering, University of Tennessee  
9 Space Institute, Tullahoma, TN 37388, USA10 <sup>4</sup>J. Crayton Pruitt Department of Biomedical Engineering, University of Florida, Gainesville, FL  
11 32611, USA12 [\\*carlos.rinaldi@ufl.edu](mailto:carlos.rinaldi@ufl.edu)

13 The potential for producing iron oxide magnetic particle imaging (MPI) tracers using an alternative  
14 synthesis method based on esterification of iron oleate with oleyl alcohol was evaluated. The  
15 defined reaction mechanism allows monitoring of reaction progress with Fourier Transform  
16 Infrared (FTIR) spectroscopy. The influence of reaction temperature and precursor flow rate on  
17 esterification reactions of Fe (II) oleate for tuning iron oxide nanoparticle size and dispersity was  
18 studied, identifying conditions for producing larger nanoparticles suitable as MPI tracers.  
19 Increasing temperature and decreasing flow rates were found to increase the resulting nanoparticle  
20 size and reduce dispersity. Furthermore, the effect of the iron source used to prepare the iron oleate  
21 precursor was evaluated by characterization of nanoparticle magnetic properties, composition, and  
22 MPI performance. Although the nature of the precursor did not appear to affect nanoparticle  
23 morphology or growth, it influenced magnetic properties and MPI performance. Saturation  
24 magnetization was close to the bulk value of magnetite and the discrepancy between physical and  
25 magnetic diameters was lowest for nanoparticles synthesized with oleates prepared using Fe (II)  
26 or Fe (III), as opposed to nanoparticles synthesized using an oleate prepared with a 1:2 molar  
27 mixture of Fe (II) and Fe (III). X-ray diffraction characterized that nanoparticles synthesized using  
28 the Fe (III) oleate are the most crystalline, followed by Fe (II) and the 1:2 Mix, respectively.  
29 Mössbauer spectroscopy was used to verify iron oxide phases, suggesting nanoparticles  
30 synthesized using the Fe (III) oleate consist of a mixture of  $\gamma$ -Fe<sub>2</sub>O<sub>3</sub> and Fe<sub>3</sub>O<sub>4</sub>, in contrast to those  
31 obtained from the Fe (II) and 1:2 Mix oleates, which consisted of a mixture of wüstite,  $\gamma$ -Fe<sub>2</sub>O<sub>3</sub>  
32 and Fe<sub>3</sub>O<sub>4</sub>. Characterization of MPI performance using a MOMENTUM™ scanner demonstrated  
33 the capability of the esterification reaction to yield high-quality monodisperse MPI tracers.



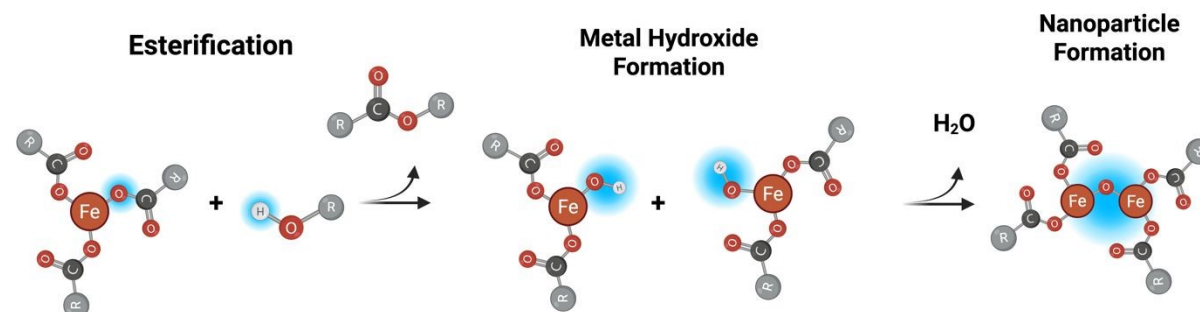
34 **Keywords:** magnetic particle imaging, iron oxide nanoparticles, superparamagnetic,  
35 esterification, synthesis

36 Iron oxide is ubiquitous in nature, but fine control at the nanoscale is crucial for maximizing  
37 its potential for many biomedical applications, including magnetic particle imaging (MPI). MPI is  
38 a rapidly developing imaging modality that relies on the nonlinear magnetization of  
39 superparamagnetic nanoparticles to generate a signal, which is proportional to the tracer mass.<sup>1</sup>  
40 This allows for quantification and visualization of tracer distribution in a volume of interest  
41 without significant tissue attenuation or applying ionizing radiation.<sup>1</sup> MPI has been applied in pre-  
42 clinical studies and holds promise for clinical applications such as cell tracking, blood pool  
43 imaging, drug delivery, and stroke detection.<sup>2-14</sup> Tracers with enhanced sensitivity and resolution  
44 are critical for advancing MPI applications,<sup>15</sup> where imaging performance is primarily governed  
45 by nanoparticle composition, size, and magnetic properties.<sup>16, 17</sup> The composition of most MPI  
46 tracers is iron oxide, and it is expected that MPI performance improves with the diameter cubed  
47 and linearly with the saturation magnetization.<sup>16, 17</sup> However, a recent study shows that reducing  
48 the discrepancy between physical and magnetic diameters is also key for enhancing MPI  
49 performance.<sup>18</sup> For decades, thermal decomposition synthesis has been the gold standard to obtain  
50 magnetic nanoparticles suitable for applications that require fine control over nanoparticle size,  
51 shape, and properties, including in producing high-quality MPI tracers.<sup>4, 11, 13, 19-25</sup> However,  
52 common challenges include formation of mixed iron oxide phases, use of toxic solvents, surface  
53 ligand effects, and high temperatures (300-350 °C) than can decompose solvents and surfactants.<sup>26</sup>  
54 The formation of wüstite, an antiferromagnetic iron oxide phase, requires synthesis  
55 modifications for oxidation to improve magnetic properties,<sup>28, 29</sup> which include post-synthesis  
56 oxidation,<sup>18, 28</sup> *in situ* synthesis oxidation,<sup>4, 29</sup> and addition of oxidizing reagents to the reaction  
57 medium, such as dibenzyl ether.<sup>30</sup> Additionally, thermal decomposition has reproducibility  
58 challenges and a poorly defined reaction mechanism, which can often hinder optimization.<sup>18, 28, 31</sup>  
59 New synthesis methods that provide fine control of both physical and magnetic properties are  
60 attractive for producing new MPI tracers, as further optimization of current methods has proved to  
61 be challenging.

62 The esterification reaction of carboxylic acids with alcohols to produce organic esters at  
63 temperatures below 200 °C is widely practiced, and esters compose some of the highest volume  
64 of industrial organic compounds produced.<sup>32</sup> More recently, conversion of metal carboxylates to



metal hydroxides through esterification in neat alcohol was demonstrated to produce another desirable product – metal oxide nanoparticles.<sup>33</sup> A slow precursor injection technique was implemented to enable production of metal oxide nanoparticles with controlled size.<sup>33, 34</sup> This approach is similar to a semi-batch thermal decomposition synthesis,<sup>35</sup> reported to afford better control of nanoparticle properties, albeit at lower temperatures such that thermal decomposition of the precursors should be negligible. Prior work with the esterification synthesis has focused on indium oxide ( $\text{In}_2\text{O}_3$ ), with some reports of other metal oxides (e.g.,  $\gamma\text{-Fe}_2\text{O}_3$ ,  $\text{Mn}_3\text{O}_4$ ,  $\text{CoO}$ ,  $\text{ZnO}$ ) at temperatures below 290 °C, all resulting in oleic acid-stabilized nanoparticles.<sup>34, 36-44</sup> For the synthesis of iron oxide nanoparticles, the reaction mechanism involves esterification of iron oleate and oleyl alcohol, catalyzed by the metal ion, producing the ester oleyl oleate and metal hydroxides (**Scheme 1**). The hydroxyl groups then undergo a dehydration reaction, producing water as a side-product and forming metal oxygen bonds (Fe-O-Fe) that initiate nanoparticle formation. Finally, the remaining oleate ligands on the nanoparticle surface also undergo esterification reactions with oleyl alcohol to further grow the nanoparticle. Removing the water produced is crucial, as it can accelerate metal carboxylate hydrolysis, causing uncontrolled growth and precipitation.<sup>34</sup> Also, because esterification reactions are equilibrium-limited, removal of water and excess of alcohol is desirable in driving the esterification reaction forward.<sup>32</sup> An advantage of this synthesis method is the well-defined reaction mechanism that incorporates oxygen, potentially eliminating the need for oxidation treatments needed with the thermal decomposition synthesis. Additionally, the reaction progress can be monitored via Fourier transform infrared (FTIR) spectroscopy. Authors have called this a “living nanoparticle synthesis”, similar to polymerization reactions, as it can be stopped and restarted by controlling the precursor addition.<sup>36, 45</sup> This continuous synthesis method also provides fast nanoparticle formation, within 60 seconds of precursor addition at 230 °C.<sup>34</sup>



89 **Scheme 1. Reaction mechanism for esterification synthesis of iron oxide nanoparticles**

90 Studies of the synthesis of  $\text{In}_2\text{O}_3$  have demonstrated that nanoparticle size and uniformity  
91 can be increased through tailored reaction conditions, such as increasing reaction temperature from  
92 230 °C to 290 °C and lowering precursor flow rate.<sup>40</sup> Others have shown that surface reactivity of  
93 nanoparticles is influenced by the choice of surface capping agent, which in turn affects  
94 nanoparticle formation and growth. For example, for  $\text{In}_2\text{O}_3$  at 290 °C, switching oleyl alcohol to  
95 oleylamine results in faster amidation reactions, which results in rapid generation of reactive metal  
96 precursors and larger nanoparticles.<sup>44</sup> The esterification synthesis method also yields precise  
97 control for doped  $\text{In}_2\text{O}_3$  nanoparticles, which is challenging in thermal decomposition due to  
98 differences in decomposition temperatures and reactivities of different metal precursors.<sup>36, 37</sup> Thus  
99 far, only a few studies have focused on synthesis of iron oxide.<sup>38, 39, 41, 42</sup> Importantly, intrinsic  
100 magnetic properties of iron oxide nanoparticles produced via esterification reactions remain  
101 largely unreported, as is their characterization for specific applications, including MPI.

102 The nature of the iron oleate precursor used has been shown to affect nanoparticle properties in  
103 both the thermal decomposition<sup>28, 35, 46-48</sup> and esterification<sup>41</sup> synthesis literature. This is not  
104 surprising, as early studies in thermal decomposition used iron pentacarbonate<sup>49, 50</sup> or iron  
105 acetylacetone<sup>51, 52</sup> salts directly in a batch reactor, but preparing iron oleate precursor as an  
106 intermediate has provided finer control.<sup>26, 35, 53</sup> The influence of iron oleate structure, binding  
107 mode, oleic acid content, and purification treatments have been shown to affect resulting  
108 nanoparticle properties.<sup>28, 46</sup> Hence, a method was developed for a reproducible synthesis of iron  
109 oleate from Fe (III) acetylacetone at 325 °C with precise iron concentration that can be used  
110 without further purification steps.<sup>35</sup> This oleate has been used to produce magnetite MPI tracers  
111 via thermal decomposition with oxidation treatments,<sup>4, 18, 29</sup> motivating comparison to the standard  
112 iron oleate precursor primarily used in the esterification synthesis literature, prepared from Fe (II)  
113 acetate at 150 °C.<sup>34, 38, 39, 41, 42</sup> The effect of iron precursor ligation and oxidation state on iron oxide  
114 nanoparticle synthesis via the esterification route has been explored at low temperatures of  
115 nanoparticle synthesis (230 °C) and precursor synthesis (150 °C).<sup>41</sup> Fe (II) acetate has been the  
116 primary salt used for preparing the iron oleate precursor for the esterification synthesis, and  
117 nanoparticles produced using an Fe (III) acetylacetone had twin defects.<sup>41</sup> Although a higher  
118 temperature for Fe (III) precursor synthesis (190 °C) led to fewer twin defects, this route was not  
119 pursued due to the likeliness of reducing the iron, a possibility previously demonstrated by Kemp



120 *et al.*<sup>28</sup> Plummer *et al.* state that after ~ 3 mmol of Fe addition with the Fe (II) oleate, nanocrystals  
121 became highly polydisperse and irreproducible.<sup>41</sup> Therefore, to achieve larger sizes, an Fe (II) and  
122 Fe (III) precursor was obtained by mixing the two precursors at a 1:2 molar ratio, corresponding  
123 to the stoichiometric Fe ratio in magnetite. Addition of 20 mmol of Fe from the mixed oleate at  
124 230 °C resulted in 19 nm nanoparticles, but extending size beyond that faced issues of dispersion  
125 after purification.<sup>41</sup>

126 Here we report a series of studies using the esterification synthesis route to synthesize iron  
127 oxide nanoparticles with sizes and magnetic properties suitable for use as tracers in MPI. The  
128 effects of higher reaction temperatures (290 °C to 350 °C) and lower precursor flow rates (0.025  
129 mmol/min to 2.5 mmol/min) were evaluated to identify conditions resulting in iron oxide  
130 nanoparticles of ~20 nm diameter. Nanoparticles obtained under similar synthesis conditions using  
131 Fe (II) and Fe (III) oleates, as well as another prepared by a 1:2 mixture of them, were characterized  
132 physically, magnetically and in terms of their MPI performance.

### 133 **Results and Discussion**

#### 134 **Low temperature (290 °C) esterification of Fe (II) oleate yielded iron oxide nanoparticles 135 that were too small to be effective MPI tracers.**

136 The esterification synthesis of metal oxide nanoparticles has been reported for a range of  
137 temperatures (230-290 °C) and precursor flow rates (0.17-0.35 mL/min). Although the influence  
138 of these parameters has only been studied for indium oxide nanoparticles,<sup>40</sup> these studies suggest  
139 that higher temperatures and lower flow rates yield larger and more uniform particles. As such, we  
140 initially evaluated the esterification synthesis of iron oxide at a temperature of 290 °C and flow  
141 rate of 0.2 mL/min, as these were at the high range of temperature and low range of flow rate  
142 evaluated for indium oxide nanoparticles.<sup>40</sup>

143 Fourier transform infrared spectroscopy (FTIR) of reaction aliquots (**Figure 1A**) facilitates  
144 tracking of the reaction progress (**Figure 1B**), revealing a halt in the production of esters and the  
145 consumption of the iron oleate precursor at around 60 min, which corresponds to the addition of 6  
146 mmol<sub>Fe</sub>. After the growth region denoted in **Figure 1B (i)**, ester peaks decrease in region **(ii)** most  
147 likely due to decomposition, as the decomposition temperature of the ester oleyl oleate is 250-  
148 300 °C.<sup>54</sup> Additionally, in region **(ii)** the Fe-oleate COO peak starts to increase suggesting it is  
149 accumulating in the reactor. This is to be expected if alcohol has been depleted, halting the



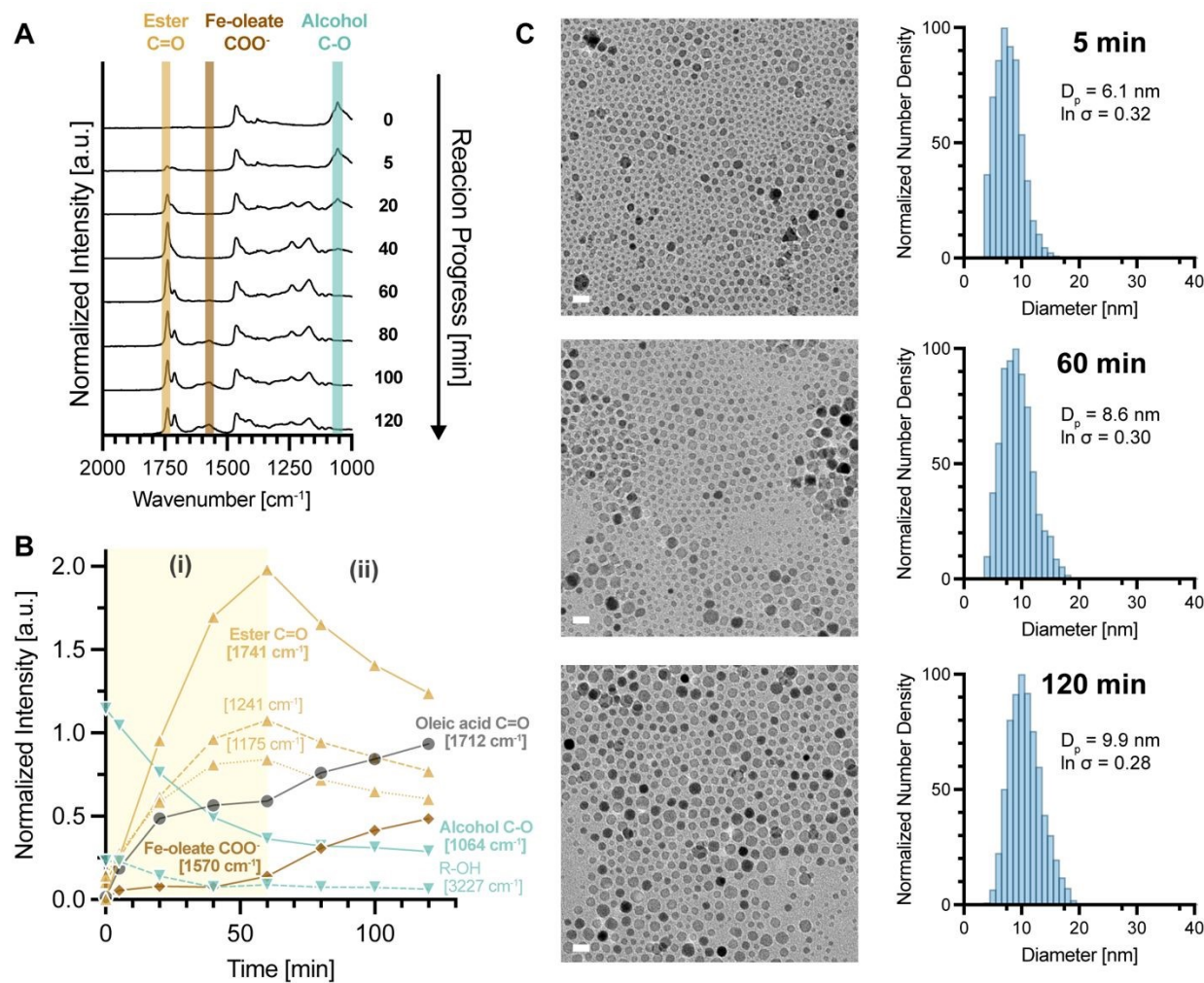
150 esterification reactions. The resulting nanoparticles were characterized physically via transmission  
151 electron microscopy (TEM) to obtain the size distributions shown in **Figure 1C**, showing that  
152 nanoparticle formation occurs early in the reaction, with a median diameter of 6 nm after 5 minutes,  
153 in contrast to thermal decomposition that may require a longer period before nanoparticles are  
154 observed.<sup>35, 55, 56</sup> After 60 min of reaction (6 mmol<sub>Fe</sub>), corresponding to the maximum for the ester  
155 peak observed in the FTIR (**Figure 1A** and **B**), the nanoparticles reach a median diameter of 8.6  
156 nm (**Figure 1C**). Further addition to 12 mmol<sub>Fe</sub> produced polydisperse nanoparticles of ~10 nm  
157 (**Figure 1C** and **Figure S1**). Under similar conditions, Plummer *et al.* reported that particles  
158 become highly polydisperse after addition of 3 mmol<sub>Fe</sub>.<sup>41</sup> We observe polydisperse nanoparticles  
159 from the first aliquot at 5 min, which corresponds to addition of 0.5 mmol<sub>Fe</sub>. Further, the 10 nm  
160 particle size obtained is not suitable to be a high-quality single core MPI tracer.<sup>17</sup>

161



article, published on 08 January 2026. Downloaded on 1/10/2026 9:58:11 AM.  
This article is licensed under a Creative Commons Attribution-NonCommercial 3.0 Unported Licence.

Open Access  
(cc) BY-NC



163 **Figure 1. Low temperature esterification of Fe (II) oleate for synthesis of iron oxide**  
164 **nanoparticles at 290 °C and a precursor addition rate of 0.1 mmol/min yields particles that**  
165 **are too small to be effective MPI tracers.** (A) Fourier Transform Infrared (FTIR) facilitates  
166 tracking of reaction progress, as the main peaks for the reagents (iron oleate and oleyl alcohol) and  
167 the ester product can be obtained from reaction aliquots. (B) Tracking FTIR intensity over reaction  
168 time demonstrates ester formation (yellow) and alcohol consumption (teal) in region (i) with the  
169 addition of 6 mmol of Fe. Further addition, results in iron oleate (brown) accumulation due to the  
170 alcohol depletion observed in region (ii). (C) Physical size distributions obtained from analysis of  
171 transmission electron microscopy (TEM) images show that polydisperse particles of ~ 6 nm  
172 quickly form after 5 min of reaction and grow to a size of ~ 10 nm after 120 min and 12 mmol Fe  
173 is added. Scale bars are 20 nm.  
174

175 **Tuning esterification of Fe (II) oleate reaction temperature and precursor flow rate yields**  
176 **iron oxide nanoparticles with diameters suitable for use as MPI tracers.**

177 Temperature and precursor flow rate have been shown to significantly affect indium oxide  
178 nanoparticle growth, influencing their size, shape, and quality.<sup>40</sup> Along with the desire to further  
179 increase nanoparticle size, this motivated a study to explore the effect of temperature and flow rate  
180 for the synthesis of iron oxide nanoparticles with addition of 1 mmol<sub>Fe</sub>. The esterification reaction  
181 has been primarily conducted at temperatures between 230–290 °C to mitigate any reducing effects  
182 that can occur at higher temperatures and avoid thermal decomposition.<sup>34, 41</sup> However, higher  
183 temperatures are typically used for the thermal decomposition of iron oleate,<sup>4, 18, 26, 28, 29, 35, 46, 53, 57</sup> motivating us to study higher temperatures in the esterification synthesis. Increasing temperature  
184 from 290 °C to 350 °C resulted in an increase in iron oxide nanoparticle diameter from 6 to 9 nm  
185 and a decrease in the geometric deviation ( $\ln \sigma_p$ ) after adding 1 mmol<sub>Fe</sub> (**Figure 2A** and **Figure**  
186 **S2**). These results agree with trends reported in a study of indium oxide esterification synthesis,  
187 where larger nanoparticles with narrower size distributions were observed at 290 °C, compared to  
188 lower temperatures.<sup>40</sup>

190 Since larger nanoparticles were observed at 350 °C, longer reactions were evaluated at this  
191 temperature. A lower flow rate of 0.05 mmol<sub>Fe</sub>/min was chosen based on studies with indium  
192 oxide.<sup>40</sup> However, attempts to carry out longer reactions at 350 °C proved to be difficult, as FTIR  
193 tracking shows depletion of alcohol after 25 min of reaction (**Figure S3A**). This is much faster  
194 than the 60 min observed for the synthesis at 290 °C (**Figure 1**). Still, larger (~13 nm) and more  
195 uniform size ( $\ln \sigma_p = 0.1$ ) nanoparticles were obtained using significantly less iron (**Figure S3B**).  
196 Precursor addition was halted after 25 min (1.25 mmol<sub>Fe</sub>) and alcohol was replenished by adding  
197 13 mL of oleyl alcohol at 0.35 mL/min, which was the original volume in the reactor. Yet, this  
198 was only partially effective, as FTIR (**Figure S3A**) shows a low amount of alcohol in the reactor  
199 at the end of alcohol addition (ii), possibly because of boil-off or decomposition. Nevertheless, the  
200 particle size analysis (**Figure S3B**) demonstrates that nanoparticle size and distribution remain  
201 consistent, showing nanoparticle growth stopped once precursor addition was halted. Adding a  
202 condenser to reduce oleyl alcohol boil-off resulted in water condensation, leading to a less uniform  
203 final nanoparticle product (**Figure S3B**). These studies at 350 °C suggested that although  
204 increasing temperature yields larger nanoparticles with narrower size distributions, further growth



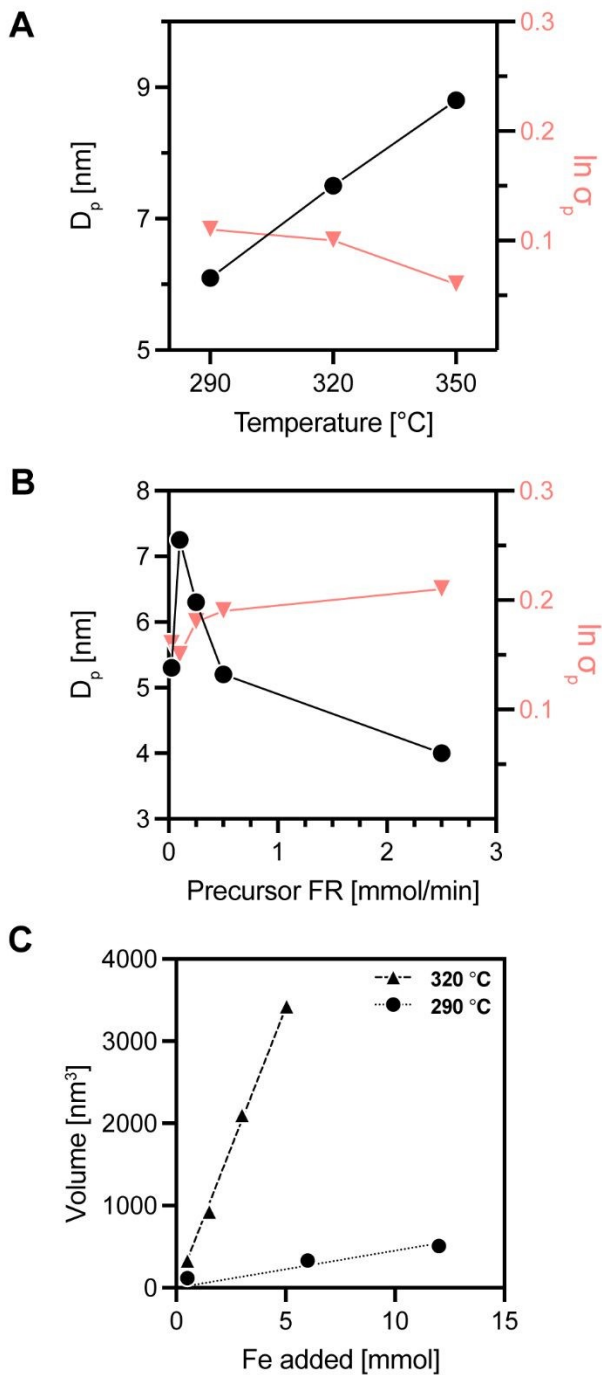
205 is limited due to depletion of oleyl alcohol, which has a boiling point of 333 °C and starts  
206 decomposing at lower temperatures.<sup>54</sup> Based on these observations, subsequent studies were  
207 performed at a synthesis temperature of 320 °C.

208 Next, the influence of iron oleate precursor addition rate was evaluated at 320 °C (**Figure**  
209 **2B**) with addition of 1 mmol<sub>Fe</sub> at various flow rates. The results in **Figure 2B** show that decreasing  
210 precursor flow rate resulted in an increase in nanoparticle diameter and a reduction in  
211 polydispersity (geometric deviation,  $\ln \sigma_p$ ). However, nanoparticle size increased only to a certain  
212 extent, as decreasing the flow rate further from 0.1 mmol<sub>Fe</sub>/min resulted in a reduction in  
213 nanoparticle size. Representative TEM images are shown in **Figure S4** and results for the effect  
214 of flow rate at 350 °C exhibiting the same behavior are shown in **Figure S5**. These studies suggest  
215 that esterification synthesis of iron oxide nanoparticles at 320 °C and a precursor flow rate of  
216 0.1 mmol<sub>Fe</sub>/min may be suitable to produce larger nanoparticles with narrow size distribution.

217 Finally, we evaluated nanoparticle growth for longer esterification syntheses at 290 °C and  
218 320 °C, and a precursor flow rate of 0.1 mmol<sub>Fe</sub>/min (**Figure 2C**). Both synthesis temperatures  
219 preserve the expected linear growth in nanoparticle volume with mmol<sub>Fe</sub> added to the reaction,  
220 suggesting that these grow continuously, with a larger rate of growth for nanoparticles synthesized  
221 at 320 °C. These results agree with studies of In<sub>2</sub>O<sub>3</sub> nanoparticle synthesis, where growth rate  
222 increased with increasing reaction temperature from 230 °C to 290 °C.<sup>40</sup> The synthesis at 320 °C  
223 yielded particles of ~18 nm with addition of 5 mmol<sub>Fe</sub> at 0.1 mmol<sub>Fe</sub>/min, suggesting this condition  
224 is appropriate to obtain nanoparticles that are suitable for MPI. This motivated subsequent studies  
225 using these conditions to explore other synthesis parameters.

226





227

228 **Figure 2. Higher esterification reaction temperatures and slower precursor addition rates**  
 229 **yield larger and more monodisperse nanoparticles.** Shorter reactions with addition of 1 mmol  
 230 of Fe were used to explore the influence of temperature and precursor flow rate for iron oxide  
 231 nanoparticles. (A) Increasing temperature from 290  $^{\circ}\text{C}$  to 350  $^{\circ}\text{C}$  increases physical diameter ( $D_p$ )  
 232 from 6 to 9 nm and decreases polydispersity (geometric deviation,  $\ln \sigma_p$ ) after addition of 1 mmol<sub>Fe</sub>  
 233 at a rate of 0.175 mmol<sub>Fe</sub>/min. (B) Decreasing precursor flow rate to 0.1 mmol<sub>Fe</sub>/min increases  
 234 physical diameter and decreases polydispersity after addition of 1 mmol of Fe at 320  $^{\circ}\text{C}$ . (C) A



235 longer reaction with addition of 5 mmol of Fe at 320 °C and 0.1 mmol<sub>Fe</sub>/min shows a significant  
236 increase in nanoparticle growth rate compared to the original conditions explored in Figure 1 (290  
237 °C and 0.1 mmol<sub>Fe</sub>/min).

238

239 **The nature of the iron oleate precursor did not influence nanoparticle morphology or  
240 growth trends**

241 Next, we evaluated the effect of iron oleate precursor composition, as it has been  
242 demonstrated to influence nanoparticle properties in both thermal decomposition and esterification  
243 synthesis.<sup>28, 35, 46, 48</sup> Fe (II) and Fe (III) oleates were prepared via methods corresponding to those  
244 commonly used in esterification and thermal decomposition syntheses using Fe(ac)<sub>2</sub> and Fe(acac)<sub>3</sub>,  
245 respectively. The oxidation state of iron in the salts used to prepare the iron oleates was used to  
246 label the corresponding oleates and differentiate the nanoparticles obtained using them in this  
247 study. Additionally, a mixed oleate was produced at a 1:2 molar ratio of Fe (II): Fe (III), which is  
248 labeled as the 1:2 Mix oleate. FTIR spectra of Fe (II) and Fe (III) oleates are shown in **Figure S6**,  
249 highlighting the main peaks of interest to compare them. The carboxylic acid C=O stretch of oleic  
250 acid at 1710 cm<sup>-1</sup> was used to calculate the percentage of free oleic acid in the oleate by comparing  
251 to the absorbance of pure oleic acid. The Fe (II) oleate contains 62% free oleic acid and the Fe (III)  
252 oleate contains 35% free oleic acid. The metal carboxylate IR bands were observed in the range of  
253 1650-1510 cm<sup>-1</sup> for the asymmetrical vibrations, and 1500-1375 cm<sup>-1</sup> for the symmetric  
254 vibrations.<sup>46</sup> The separation ( $\Delta v$ ) of the bands in these regions has been used to deduce the  
255 carboxylate coordination mode. The maximum peak absorbance in these regions were subtracted  
256 to obtain a  $\Delta v$  of 184 cm<sup>-1</sup> and 159 cm<sup>-1</sup> for the Fe (II) and the Fe (III) oleates, respectively, which  
257 corresponds to a bridging coordination mode. These results suggest that the Fe (II) and Fe (III)  
258 oleates contain similar metal carboxylate coordination modes but have a notable difference in their  
259 free oleic acid content. The latter is to be expected as the oleic acid to metal ratio is 6.3 and 5 for  
260 the Fe (II) and Fe (III) oleate synthesis procedures, respectively, and the stoichiometric amount  
261 required for Fe (II) and Fe (III) salts is different as well.

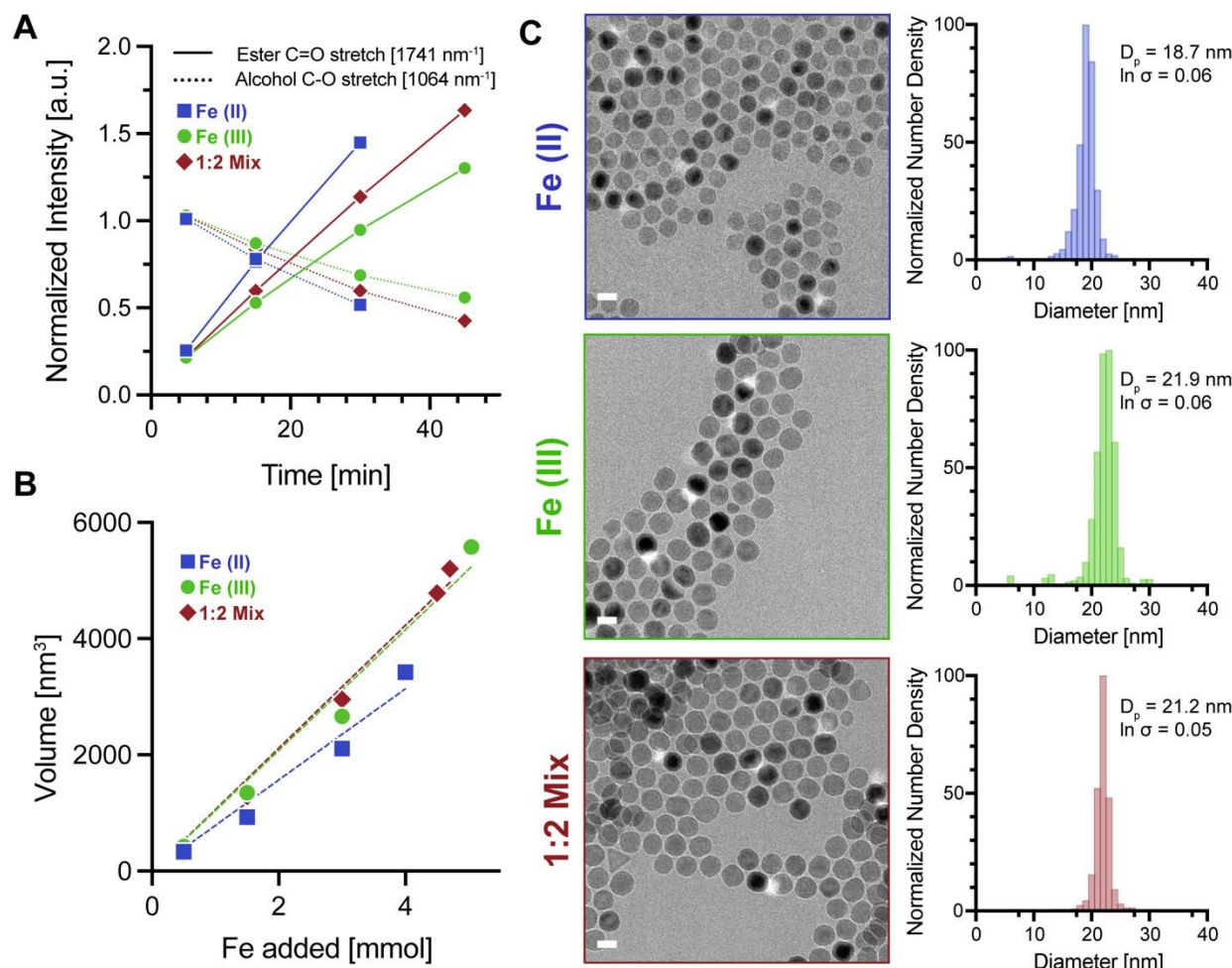
262 The same volume of Fe (II) and Fe (III) precursors (8 mL) was added to each reactor at  
263 320 °C to test the influence of iron oleate precursor on nanoparticle properties. Due to their  
264 different iron concentrations (0.5 M for the Fe (II) oleate, 0.63 M for the Fe (III) oleate, and 0.58  
265 M for the 1:2 Mix oleate), the number of moles of Fe used in the reaction varied from 4 to 5



266 mmol<sub>Fe</sub>. Comparing trends in FTIR peaks associated with ester formation and oleyl alcohol  
267 consumption (**Figure 3A**) suggests similar rates of ester formation and alcohol consumption for  
268 the three oleates. Furthermore, similar nanoparticle growth trends were observed for the three  
269 oleates (**Figure 3B**). Finally, similar nanoparticle morphology and size distributions were observed  
270 for the final product of each synthesis (**Figure 3C** and **Figure S6**). Although the median physical  
271 diameter for the nanoparticles obtained using the Fe (II) oleate was smaller (18.7 nm) than that  
272 obtained with the Fe (III) and 1:2 Mix oleate (21.9 nm and 21.2 nm), it must be noted that there is  
273 a 1 mmol<sub>Fe</sub> difference in the iron added to that reaction compared to the Fe (III) oleate. These  
274 observations suggest that esterification synthesis at 320 °C and 0.1 mmol<sub>Fe</sub>/min using these three  
275 oleates results in similar nanoparticle morphologies, growth trends, and size distributions.

276



277  
278279  
280  
281  
282  
283  
284  
285  
286

**Figure 3. Esterification synthesis of iron oxide nanoparticles using iron oleates prepared from different iron salts resulted in similar nanoparticle growth trends and morphologies.** (A) FTIR tracking of the main ester and alcohol peaks show similar behavior for reactions using the Fe (II), Fe (III), and 1:2 Mix oleates. (B) Similar trends in nanoparticle growth were observed for reactions with all three oleates. (C) TEM images and corresponding physical diameter distribution histograms show similar size, shape, and distribution of nanoparticles for reactions with all three oleates. Scale bars are 20 nm.

287

## 288 The nature of the iron oleate precursor influences the magnetic properties and composition 289 of iron oxide nanoparticles obtained via esterification synthesis

290 Nanoparticle composition and magnetic properties influence MPI performance,<sup>17</sup> hence  
291 further characterization of nanoparticles obtained via esterification synthesis using the three  
292 oleates is crucial. The basic adiabatic theory of x-space MPI suggests that signal strength and

resolution both improve with increasing initial magnetic susceptibility and saturation magnetization of the nanoparticle tracer.<sup>16, 17</sup> According to the Langevin model for superparamagnetism, the initial susceptibility increases with the cube of the nanoparticle diameter. Additionally, prior work highlights the importance of minimizing discrepancy between physical and magnetic diameters for improving MPI performance.<sup>18</sup>

Magnetic properties were evaluated by measuring magnetization of nD-PEG coated nanoparticles in water as a function of applied magnetic field at 300 K (**Figure 4A** and **Figure S7**). All three nanoparticles display superparamagnetic behavior, with no observed hysteresis and with magnetic saturation. The initial susceptibility was largest for nanoparticles synthesized using the Fe (III) oleate, followed by nanoparticles synthesized using the Fe (II) oleate, and then nanoparticles synthesized using the 1:2 Mix oleate. Magnetic diameters ( $D_m$ ) were estimated by fitting the magnetization measurements to the Langevin function, weighted by a lognormal diameter distribution. Results in **Table 1** show that nanoparticles synthesized using the Fe (III) oleate possess the largest magnetic diameter, 20 nm, compared to those synthesized using the Fe (II) and 1:2 Mix oleates, with 16 nm and 12.5 nm, respectively. The saturation specific magnetizations for all three nanoparticles are shown in **Table 1** and are close to the value for bulk magnetite ( $120 \text{ A m}^2/\text{kg}_{\text{Fe}}$ ). The nanoparticles obtained using the Fe (III) oleate had the smallest discrepancy between physical and magnetic diameters (1.9 nm), and a high saturation magnetization ( $128 \text{ A m}^2/\text{kg}_{\text{Fe}}$ ). Next, the nanoparticles obtained with the Fe (II) oleate had similarly high saturation magnetization ( $127 \text{ A m}^2/\text{kg}_{\text{Fe}}$ ), but a larger discrepancy between physical and magnetic diameters (2.7 nm). Finally, the nanoparticles synthesized using the 1:2 Mix oleate had a high (but comparably lower) saturation magnetization ( $115 \text{ A m}^2/\text{kg}_{\text{Fe}}$ ), and the largest discrepancy between physical and magnetic diameters (8.7 nm). This discrepancy between physical and magnetic diameters was observed in 20 nm commercial nanoparticles from Ocean Nanotech and has been studied in the thermal decomposition synthesis, where an oxidizing agent is needed to reduce the so-called “magnetic dead layer”.<sup>29</sup> Sub-10 nm iron oxide particles prepared from the Fe (II) oleate via the esterification synthesis at lower temperature (230 °C) were previously shown to have very similar physical and magnetic diameters,<sup>39</sup> but a larger discrepancy is observed for the larger nanoparticles obtained at the reaction conditions of this study.

Iron oxide phases were identified using X-ray diffraction (XRD), which show broader peaks for nanoparticles synthesized using the Fe (II) and 1:2 Mix oleates, relative to the sharper peaks



for nanoparticles synthesized using the Fe (III) oleate (**Figure 4B**). This difference in broadening is most clearly observed in peaks at higher angles (50-65 °). The locations and relative intensities of the most prominent peaks were consistent with magnetite ( $Fe_3O_4$ ) and maghemite ( $Fe_2O_3$ ) crystal structures. However, these two phases are difficult to distinguish due to their similar XRD patterns and, further, the broadening that results from the nanometer-scale sizes. Despite their similarities and peak broadening, there was evidence of coexistence of the magnetite and maghemite phases in the Fe (II) and 1:2 Mix samples. The shoulder in the 35 ° peak and the shift in the 44 ° peak indicate a mixed phase product, but no peaks indicate the formation of the wüstite ( $FeO$ ) phase. The absence of  $FeO$  is an advantage to thermal decomposition methods, where the formation of this nonmagnetic phase has been demonstrated before being oxidized to  $Fe_3O_4$  or  $Fe_2O_3$ .<sup>46, 58-60</sup> However, detection of small impurities or other iron oxide phases can be difficult due to overlapping peaks, along with peak broadening. Minor peaks observed at 27, 32, and 51 ° suggest iron oxide hydroxide species, but cannot be fully resolved and identified at the measurement conditions. Previous XPS characterization reported the presence of surface hydroxyls on the nanoparticle along with oleate ligands at lower synthesis temperatures.<sup>34</sup> These observations can motivate further characterization of the nanoparticle surface to investigate the potential of forming iron oxide hydroxides with long-range ordering detectable by XRD. Crystallite sizes estimated using Scherrer's equation and the main peaks are shown in **Table 1** and were largest for the nanoparticles obtained using the Fe (III) oleate (17.1 nm), followed by those synthesized using the 1:2 Mix oleate (14.8 nm), and those synthesized using the Fe (II) oleate (13.1 nm). Crystal sizes determined from XRD have been previously found to correlate with the magnetic diameters estimated from analysis of the equilibrium magnetization curves, as the magnetic dipole is a result of the crystal's long-range ferroic ordering.<sup>29</sup> This motivated comparison in this study, where the crystallite sizes ( $D_{XRD}$ ) did not match the magnetic sizes ( $D_m$ ). However, the discrepancy between physical and magnetic diameters ( $D_p - D_m$ ) correlates with the discrepancy between physical and crystal sizes ( $D_p - D_{XRD}$ ) (**Table 1**), which suggests one can be informative of the other.

Further characterization using  $^{57}Fe$  Mössbauer spectroscopy probes the environment of iron atoms, providing information on oxidation states and phase compositions. Stacked Mössbauer spectra of samples measured at 293 K are displayed in **Figure 4C**, with hyperfine fit parameters in **Table S1**. All samples exhibit two magnetically split spinel sextets: a tetrahedral A-site  $Fe^{3+}$



355 component (teal) and an octahedral B-site valence-averaged ( $Fe^{2.5+}$ ) component characteristic of  
356 magnetite above the Verwey transition (pink). In addition, the nanoparticles obtained using the Fe  
357 (II) and 1:2 Mix oleates show a central  $Fe^{2+}$  doublet (orange) attributed to wüstite (FeO), whereas  
358 the Fe(III) oleate sample does not. Stacked spectra at 6 K are displayed in **Figure 4D**, with fit  
359 parameters in **Table S2**. At low temperature, all samples display three spinel sextets: tetrahedral  
360 A site  $Fe^{3+}$  (teal), octahedral B site  $Fe^{3+}$  (pink), and a distinct octahedral B site  $Fe^{2+}$  sextet (purple)  
361 that is indicative of magnetite. Additionally, sextets assigned to wüstite  $Fe^{2+}$  (orange) were  
362 observed for the Fe (II) and 1:2 Mix oleate samples. Fe-atom fractions corresponding to magnetite,  
363 maghemite, and wüstite (Table 1) were from the 293 K site areas. The wüstite fraction was taken  
364 from its doublet area (Site 3 in **Table S1**) and excluded from the spinel total. The maghemite  
365 fraction was calculated by subtracting half of the area assigned to the  $Fe^{2.5+}$  valence averaged site  
366 (Site 2 in **Table S1**) from the area assigned to Magnetite A (tetrahedral) site  $Fe^{3+}$  and Maghemite  
367 A & B sites  $Fe^{3+}$  (Site 1 in **Table S2**). Estimated maghemite contents for each sample are indicated  
368 in **Table 1**. These estimates indicate that nanoparticles synthesized using the Fe(III) oleate  
369 correspond to a mixture of magnetite and maghemite, whereas the nanoparticles synthesized using  
370 the Fe(II) and 1:2 Mix oleates contain wüstite and a mixture of magnetite and maghemite, with a  
371 spinel fraction dominated by maghemite.

372 The oxidation state of the Fe oleate precursors prepared in this study were not investigated,  
373 but oxidative decarboxylation of the oleate has been reported to reduce Fe (III) to Fe (II) starting  
374 at temperatures below 180 °C.<sup>28</sup> Although the oleate precursor is dripped into the reactor for the  
375 esterification synthesis, the Fe (III) oleate synthesis method used requires heating it over 300 °C,  
376 which could cause reduction to Fe (II). This mechanism could explain formation of  $Fe_3O_4$  from  
377 the Fe (III) oleate precursor, but further investigation would be necessary.

378 Prior studies have demonstrated partial oxidation of magnetite nanoparticles when bubbling  
379 with air or  $O_2$ , with the extent of oxidation being dependent on the ligand at the particle surface  
380 and being minimal for oleic acid coated particles and maximal for particles coated with  
381 tetramethylammonium hydroxide.<sup>61</sup> During our ligand exchange at 101°C the particles are  
382 suspended in toluene, there is no bubbled oxygen source, and are coated initially with oleic acid  
383 and eventually with the much stronger capping agent nitroDOPA-PEG. Because of this  
384 combination of low oxygen solubility in toluene, no active source of oxygen, and particles coated

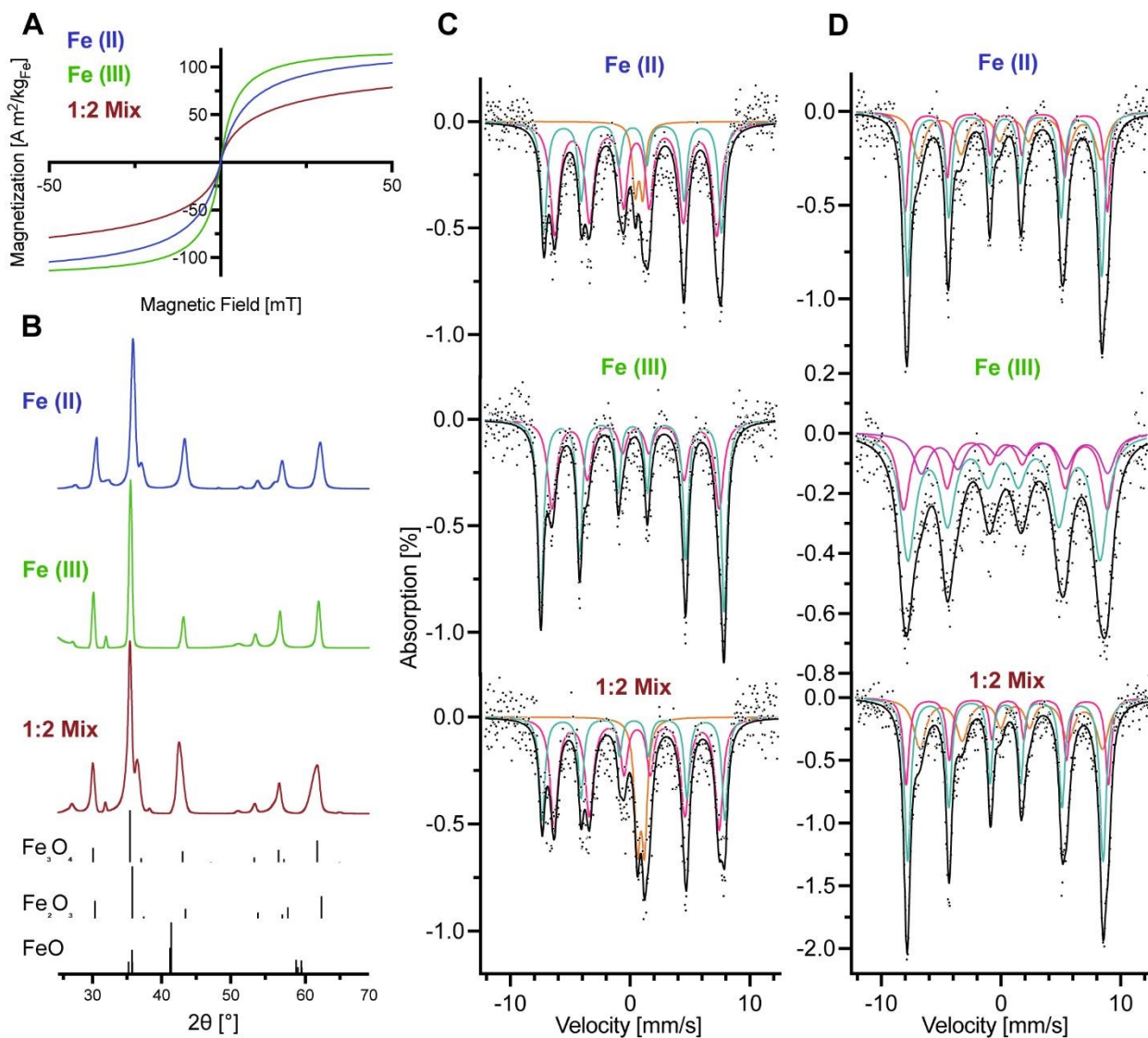
385 with strong ligands we do not expect significant oxidation during the ligand exchange process and  
386 leave study of this potential phenomenon to future work.

387 Regardless, the Fe (III) oleate tailored for thermal decomposition yields highly crystalline  
388 magnetic nanoparticles obtained by esterification synthesis at high temperature. Optimizing both  
389 reaction conditions and iron sources eliminated the need to synthesize both Fe (II) and Fe (III)  
390 precursors to yield larger  $\text{Fe}_3\text{O}_4$  nanoparticles. Although particle growth and morphology were  
391 similar using the three oleates, they differed in their magnetic properties, crystallinity, and  
392 Mössbauer spectra. The high saturation magnetization and crystallinity, along with the small  
393 discrepancy between physical and magnetic diameters, suggests the nanoparticles synthesized  
394 from the Fe (II) and Fe (III) oleates have potential as high sensitivity and resolution MPI tracers.

395

396





397  
398 **Figure 4. Different mixtures of iron oxide phases are observed for esterification synthesis**  
399 **using various iron oleate precursors (Fe (II), Fe (III), and 1:2 Mix).** (A) Magnetization vs  
400 magnetic field curves at 300 K of nD-PEG coated nanoparticles used to estimate magnetic  
401 diameters ( $D_m$ ) and saturation magnetizations ( $M_s$ ). (B) X-ray diffraction (XRD) at 1.5 Å shows  
402 broad magnetite ( $Fe_3O_4$ ) or maghemite ( $\gamma-Fe_2O_3$ ) peaks for Fe (II) and 1:2 Mix samples, as these  
403 are indistinguishable with XRD, meanwhile, sharper peaks were obtained for the Fe (III) sample.  
404 (C) Mössbauer spectroscopy at 293 K, with fitted subspectra corresponding to magnetite A  
405 (tetrahedral) site  $Fe^{3+}$  and maghemite A & B sites  $Fe^{3+}$  (teal sextet), magnetite B (octahedral) site  
406  $Fe^{2.5+}$  (valence averaged, pink sextet), and Wüstite ( $Fe_{1-x}O$ )  $Fe^{2+}$  site (orange doublet). (D)  
407 Mössbauer spectroscopy at 6 K, with fitted subspectra corresponding to magnetite A (tetrahedral)  
408 site  $Fe^{3+}$  and maghemite A & B sites  $Fe^{3+}$  (teal sextet), magnetite B (octahedral) site  $Fe^{3+}$  (pink  
409 sextet), magnetite B-site  $Fe^{2+}$  and wüstite ( $Fe_{1-x}O$ )  $Fe^{2+}$  site (orange sextet), and magnetite B-site  
410  $Fe^{2+}$  (purple sextet).

411

412 **Esterification synthesis yields MPI tracers with high sensitivity and resolution performance**

413 First, we evaluated the point spread function (PSF) for each nanoparticle, using the  
414 RELAX™ module in the MOMENTUM™ MPI scanner (**Figure 5A**). In the PSF, signal intensity  
415 corresponds to sensitivity and the full width half-maximum (FWHM) corresponds to resolution.  
416 Nanoparticles synthesized using the Fe (II) and Fe (III) oleates had a high signal intensity, with  
417 values of 77.4 and 108.5  $\text{mg}_{\text{Fe}}^{-1}$ , respectively. In contrast, nanoparticles synthesized using the 1:2  
418 Mix oleate had a lower sensitivity of 40.7  $\text{mg}_{\text{Fe}}^{-1}$ , which agrees with expectations based on the  
419 larger discrepancy between physical and magnetic diameters and poorer crystallinity. The  
420 nanoparticles synthesized using the Fe (II) and 1:2 Mix oleates had similar FWHM of 10.5 and  
421 10.4 mT, respectively. Nanoparticles synthesized using the Fe (III) oleate had a lower FWHM of  
422 8.6 mT, which suggests superior imaging resolution. The nanoparticles synthesized using the 1:2  
423 Mix oleate had similar magnetic properties and MPI performance as VivoTrax in our scanner,<sup>62</sup>  
424 meanwhile the nanoparticles synthesized using the Fe (II) and Fe (III) oleates had superior  
425 magnetic properties and MPI performance. Specifically, nanoparticles synthesized using the Fe  
426 (III) oleate have comparable performance to VivoTrax+, a recently developed version enhancing  
427 MPI performance to a signal intensity of 97.5  $\text{mg}_{\text{Fe}}^{-1}$  and a FWHM of 7.1 mT. These results suggest  
428 that the esterification synthesis is a valuable route for synthesizing and optimizing monodisperse  
429 MPI tracers.

430 MPI 2D standard mode scans were obtained for serial dilutions of each of the nanoparticles,  
431 resulting in the expected linear relationship between MPI signal and iron mass (**Figure 5B**). The  
432 dotted horizontal line represents the background signal of non-magnetic material based on the  
433 average signal of water samples. For nanoparticles synthesized using the Fe (II) and Fe (III)  
434 oleates, a real signal in the known location of the sample was observed down to 50  $\text{ng}_{\text{Fe}}$ , meanwhile  
435 for the nanoparticles synthesized using the 1:2 Mix oleate a real signal was distinguished down to  
436 100  $\text{ng}_{\text{Fe}}$ . **Figure 5C** shows 2D scans comparing 1  $\text{mg}_{\text{Fe}}$ , which shows the nanoparticles  
437 synthesized using the Fe (III) oleate had a brighter signal, followed by nanoparticles synthesized  
438 using the Fe (II) and 1:2 Mix oleates, respectively. To compare resolution, standard 2D imaging  
439 was used to obtain line scans of resolution phantoms separated by various distances until the signal  
440 between them has a signal higher than half of the maximum signal. This corresponds to separation  
441 of signal when the signal between the two sources is less than half the maximum (dotted line in  
442 **Figure 5D**). This allows for estimating imaging resolution, where results show that the signals



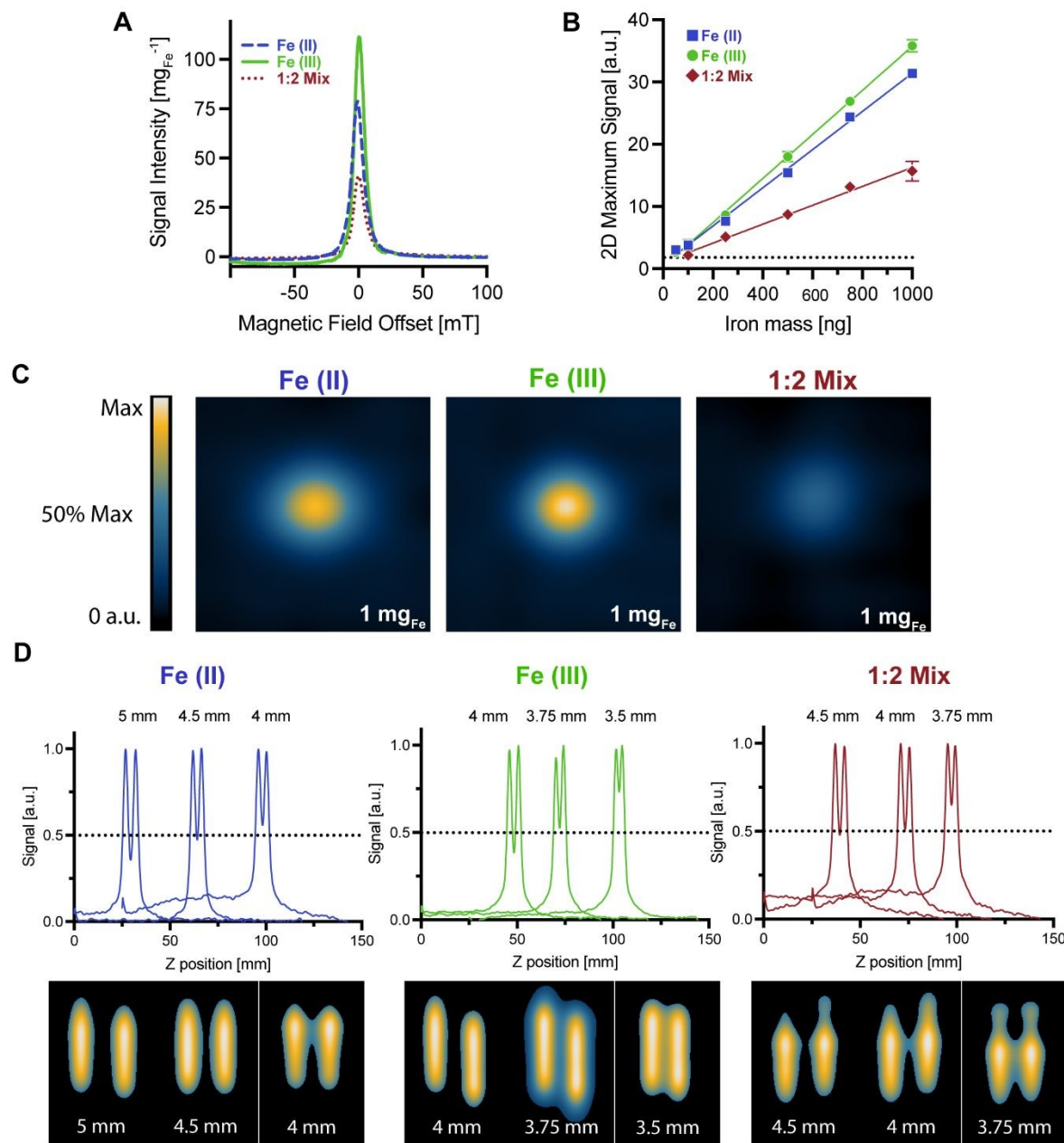
443 from the nanoparticles synthesized using the Fe (III) oleate are well separated at a distance between  
444 3.75-4 mm, meanwhile the nanoparticles synthesized using the Fe (II) and 1:2 Mix oleates require  
445 distance larger than 4 mm to have well separated signals.

446 **Table 1.** Properties obtained from characterization of iron oxide nanoparticles synthesized at 320  
447 °C using different iron oleate precursors at an addition flow rate of 0.1 mmol/min.

Properties	Fe (II)	Fe (III)	1:2 Mix
$D_p$ [nm]	18.7	21.9	21.2
$\ln \sigma_p$	0.06	0.06	0.05
$D_m$ [nm]	16	20	12.5
$\ln \sigma_m$	0.33	0.26	0.57
$D_p - D_m$	2.7	1.9	8.7
Crystal Size – $D_{XRD}$ [nm]	13.1	17.1	14.8
Crystal Size Error [nm]	0.8	0.8	0.9
$D_p - D_{XRD}$	5.6	4.8	6.4
$M_s$ [A m <sup>2</sup> /kg <sub>Fe</sub> ]	128	127	115
Fe <sub>3</sub> O <sub>4</sub> (Fe %)*	87%	63%	78%
$\gamma$ -Fe <sub>2</sub> O <sub>3</sub> (Fe %)*	4%	37%	5%
FeO (Fe %)*	9%	0%	17%
MPI Signal Intensity [a.u./mg Fe]	77.4	108.5	40.7
MPI FWHM [mT]	10.5	8.6	10.4

448 \*Based on site relative areas obtained from fitting of 293 K Mössbauer spectra.





449  
450  
451 **Figure 5. Esterification synthesis yields high-quality iron oxide MPI tracers with various**  
452 **precursors at optimized reaction conditions.** (A) Comparison of signal intensity and resolution

453 (FWHM) based on RELAX™ scans show superior performance for nanoparticles synthesized with

454 Fe (III) oleate. (B) 2D MPI scans of serial dilutions in standard mode show the expected linear

455 relationship between signal and iron mass for all samples, agreeing with the higher signal obtained

456 from RELAX™ scans for the Fe (III) sample. (C) 2D scans of 1 mg of Fe for the three tracers are

457 shown for visual comparison. (D) Line scans of linear resolution phantoms agree with expectations

458 from RELAX™ scans, showing signals of Fe (III) sample can be separated by smaller distances

459 than the Fe (II) and 1:2 Mix samples.



460

461 **Conclusions**

462 This study demonstrates the use of an esterification synthesis method to obtain high-quality  
463 MPI tracers with fine control of nanoparticle size, properties, and composition, highlighting an  
464 alternative approach to the often-used thermal decomposition synthesis. The results show that  
465 tracking the reaction progress with FTIR can facilitate optimization and tuning of reaction  
466 conditions for new applications. Nanoparticle growth curves demonstrate continuous growth,  
467 which allows for control of nanoparticle size. Comparison of different iron oleates demonstrated  
468 limited effects on nanoparticle physical properties, but more strongly influenced magnetic  
469 properties and phase composition. Crystal size estimates and quantification of  $\text{Fe}_3\text{O}_4:\gamma\text{-Fe}_2\text{O}_3$   
470 ratios with XRD and Mössbauer spectroscopy, respectively, suggest that nanoparticles synthesized  
471 using the Fe (III) oleate were the most crystalline and consisted of a mixture of maghemite and  
472 magnetite, meanwhile Fe (II) and the 1:2 Mix oleate resulted in a mixture of wüstite, magnetite,  
473 and maghemite. All samples exhibit decent performance as MPI tracers, with the nanoparticles  
474 synthesized with the Fe (III) oleate having the best MPI performance in this study, comparable to  
475 that of Vivotrax+. The synthesis of magnetic nanoparticles mediated by esterification reactions in  
476 a biocompatible solvent shows tremendous potential for MPI, along with other biomedical  
477 applications. The ability to track reaction progress via FTIR and the incorporation of oxygen in  
478 the reaction mechanism makes this synthesis method attractive for further optimization of size and  
479 composition with fine control of nanoparticle properties.

480 **Materials and Methods**481 **Materials**

482 Iron(III) acetylacetone (>98% pure) was purchased from TCI American (Portland, OR). Iron(II)  
483 acetate (95%), oleic acid (90% technical grade), and diethyl ether (certified ACS) were purchased  
484 from Sigma-Aldrich (St. Louis, MO). Oleyl alcohol (80-85% technical grade), hexane (>98.5%,  
485 certified ACS), toluene (>99.5%, certified ACS), ethanol (200 proof), and tetrahydrofuran (THF,  
486 99.8% for HPLC) were purchased from Thermo Fisher Scientific (Waltham, MA). Copper  
487 transmission electron microscopy (TEM) grids (carbon film only, 200 mesh) were purchased from  
488 TED PELLA, INC (Redding, CA).



489 **Synthesis of iron (II) oleate precursor**

490 The iron (II) oleate was prepared by mixing 1.39 g of Iron(II) acetate (8 mmol) and 16 mL of oleic  
491 acid (14.24 g, 45.6 mmol based on 90% purity) in a 100 mL three neck flask. The reactor was then  
492 connected to a Schlenk line, placed in a heating mantle, and mixed using a borosilicate magnetic  
493 stir bar with a stir plate. The mixture was vacuum purged three times, holding vacuum (~0.2-0.3  
494 Torr) for 5 minutes each time and then purging with argon gas. Then, argon flow rate was set to  
495 50 sccm and the reactor was wrapped with quartz wool insulation before ramping to 150 °C. After  
496 reaching the reaction temperature, the reaction was soaked for 1 hour. Finally, the reactor was  
497 removed from the heating mantle and allowed to cool before use for nanoparticle synthesis. A drop  
498 of the iron oleate was scanned via FTIR to determine the percentage of free oleic acid and identify  
499 the oleate structure.

500 **Synthesis of iron (III) oleate precursor**

501 The iron (III) oleate was prepared according to published work with some modifications. Iron (III)  
502 acetylacetone (22.38 g, 63.36 mmol) was combined with oleic acid (89.48 g, 316.80 mmol) in a  
503 1:5 molar ratio inside a 500 mL 3-neck round-bottom flask. The flask was then introduced into a  
504 molten metal bath set at 110 °C, with a condenser, thermocouple, and overhead stirrer in the 3  
505 necks. The condenser was connected to a chiller set to 12 °C and attached to the right neck of the  
506 reactor. The overhead stirrer, set up in the middle neck, was set to a rate of 350 rpm. The  
507 thermocouple and gas flow needle were held by a septum in the left neck with the argon gas flow  
508 set to 100 sccm. Once the equipment was set up, the molten metal bath was ramped up in  
509 temperature to a set point of 325 °C at a rate of 6.2 °C/min. After the reaction crossed 300 °C,  
510 close monitoring required taking aliquots with a syringe and stainless-steel needle through the  
511 septum in the left neck. FTIR was used to scan aliquots in real time and determine the reaction end  
512 point, controlling the percentage of free oleic acid left in the oleate. Once the free oleic acid present  
513 in the precursor mixture was estimated to be close to 35%, the reactor was removed from the heater  
514 and allowed to cool to room temperature before leaving it under vacuum overnight, prior to iron  
515 oxide nanoparticle synthesis the next day.

516 **Synthesis of iron oxide nanoparticles**

517 The setup for the synthesis of iron oxide nanoparticles through esterification reactions is shown in  
518 Scheme S1. First, 13 mL of oleyl alcohol (34.98 mmol based on 85% purity) were added to a 100



519 mL three-neck flask, placed in a heating mantle, and mixed using a borosilicate glass coated  
520 magnetic stir bar with a stir plate. The reactor's left neck was connected to the Schlenk line, and  
521 the middle neck had a rubber septum with a thermocouple. A glass stopper was added to the right  
522 neck of the reactor before starting a vacuum treatment for 1 hour while heating to 140 °C. After  
523 the vacuum treatment, the reactor was purged with Argon. The flow rate of Argon through the  
524 reactor was set to 100 sccm using a mass flow controller, and the glass stopper in the right neck of  
525 the reactor was removed. Then, the reactor was wrapped with quartz wool insulation before heating  
526 to the desired reaction temperature (290-350 °C tested in these studies). After reaching the reaction  
527 temperature in the reactor, the iron oleate was dripped from the middle neck of the reactor at a  
528 controlled flow rate using a syringe pump. The range of 0.05-5 mL/min (0.025-2.5 mmol/min) was  
529 tested in these studies. For the shorter experiments adding 1 mmol<sub>Fe</sub> no aliquots were taken, but  
530 for longer reactions aliquots were taken every 20 minutes for FTIR and TEM characterization.

### 531 **Nanoparticle purification**

532 Nanoparticles were purified using hexane and ethanol solvent-antisolvent washes with circular  
533 magnetic Halbach arrays to remove reaction byproducts and any remaining reagents. Synthesized  
534 nanoparticles were well homogenized after storage, and 1 mL of reaction mixture was added to a  
535 15 mL centrifuge tube. This was followed by the addition of 0.3 mL of hexane, vortexing, and  
536 addition of 1 mL of ethanol. This solution was lightly mixed before inserting into a circular  
537 Halbach array for 10 minutes. The supernatant was discarded by decanting while keeping the tube  
538 in the Halbach array, and nanoparticles were resuspended in 0.75 mL of hexane. After mixing and  
539 adding 1 µL of oleic acid to ensure none of the surface oleic acid groups are displaced, cup horn  
540 sonication was used for 1 minute at 80% amplitude. Again, 1 mL of ethanol was added to the  
541 nanoparticle solution, lightly mixed, and inserted into the Halbach array for 10 minutes. The  
542 supernatant was discarded, and the last step repeated two more times. After the final supernatant  
543 was discarded, nanoparticles were resuspended in 1 mL toluene. Aliquots were taken to perform  
544 iron quantification prior to the ligand exchange process.

### 545 **Iron quantification UV-Vis absorbance assay**

546 To quantify iron in both the nanoparticle toluene and water purified solutions, a 1-10-  
547 phenanthroline colorimetric assay was employed. First, 10 µL of the nanoparticle solution (based  
548 on this assay, [Fe] ~ 3-5 and 1-2 mg<sub>Fe</sub>/mL for toluene and water solutions, respectively) was



549 digested in 1 mL of 70 %  $\text{HNO}_3$ , prepared in triplicate, and placed in a heating block at 101 °C  
550 overnight. An aliquot (10-20  $\mu\text{L}$ ) of each digested sample was dried in a separate vial, leaving  
551 behind a crust. Then, 46  $\mu\text{L}$  of deionized water and 30  $\mu\text{L}$  of hydroxylamine hydrochloride (8 M)  
552 were added and mixed by pipetting into each sample before allowing the reaction to reduce iron  
553 for 1 h. To complex with  $\text{Fe}^{2+}$ , 49  $\mu\text{L}$  of sodium acetate (1.2 M) and 75  $\mu\text{L}$  of 1,10-phenanthroline  
554 monohydrate (13 mM) were mixed before aliquoting 100  $\mu\text{L}$  of each final sample solution into a  
555 96-well polystyrene plate for absorbance measurements at 508 nm in a SpectraMax M5 microplate  
556 reader. Concentrations for each sample were determined by relating the absorbance to a calibration  
557 curve prepared from an iron standard solution.

### 558 **nD-PEG particle coating**

559 First, 22 mg of nD-PEG (nitroDOPA-Polyethylene Glycol) was dissolved in 4.276 mL of toluene  
560 at 101 °C. The solution was homogenized and 0.724 mL of nanoparticles suspended in toluene  
561 were added (4 mg/mL concentration). Calculations were performed for a monolayer of PEG in  
562 accordance with previous work, using 5 times excess of nD-PEG.<sup>63-66</sup> The solution was  
563 ultrasonicated for 90 seconds to minimize aggregates and then left in a heating block at 101 °C for  
564 24 hours for the ligand exchange. Then, nanoparticles were separated by anti-solvent enhanced  
565 magnetic separation using diethyl ether at a 1:3 ratio and placing the vial in a circular Halbach  
566 array for 10 minutes. The supernatant was discarded, and the nanoparticles were resuspended in  
567 THF. Diethyl ether was added again at a 1:1.5 ratio before placing in the circular Halbach array  
568 for 10 minutes. This wash was repeated 4 times to remove excess nD-PEG. After the final wash,  
569 nanoparticles were resuspended in deionized water, passed through a 0.22  $\mu\text{m}$  filter to remove  
570 aggregates, and filtered using a Miltenyi Biotech LS magnetic column to further purify and  
571 concentrate the nanoparticles. Dynamic Light Scattering (DLS) measurements were used to  
572 confirm nanoparticle coating and stability in deionized water.

### 573 **Nanoparticle characterization**

#### 574 **Transmission electron microscopy**

575 Transmission electron microscopy (TEM) was used to acquire information about the size  
576 distribution of iron oxide nanoparticles. Oleic acid-stabilized particles suspended in hexane were  
577 loaded onto 200-mesh copper grids with carbon film and imaged using a FEI Talos F200i S/TEM.  
578 Images were analyzed using a custom TEM Image Analysis Graphical User Interface (GUI)



579 program in MATLAB, which was developed to perform physical analysis of particles in TEM  
 580 images based on the area segmented. We included at least 1,000 particles in the analysis to report  
 581 physical diameters ( $D_p$ ), and size distribution statistics. The number median physical diameter  
 582 ( $D_{pg}$ ) and geometric deviation ( $\ln \sigma_p$ ) of the particle size distribution were obtained by fitting the  
 583 size distribution histograms to the log-normal distribution ( $n_N(D_p)$ ):

$$n_N(D_p) = \frac{1}{\sqrt{2\pi} D_p \ln \sigma_p} \exp\left(-\frac{\ln^2 D_p / D_{pgv}}{2 \ln^2 \sigma_g}\right) \quad (1)$$

584 **Magnetometry and magnetic diameter fitting**

585 Magnetic properties were evaluated using a magnetic property measurement system (MPMS-3)  
 586 superconducting quantum interference device (SQUID) magnetometer from Quantum Design, Inc.  
 587 (Santa Clara, CA, USA). nD-PEG-coated nanoparticles were loaded in PTFE sample holders,  
 588 while suspended in 100  $\mu$ L of deionized water at concentrations from 1-2 mg<sub>F</sub>/mL. Magnetization  
 589 versus magnetic field (MH) curves were acquired at 300 K to confirm superparamagnetic behavior  
 590 (Figure S7) and fit the data to the Langevin function for superparamagnetism (equations 2-4),  
 591 weighted using a log-normal size distribution ( $n_v(D_m)$ ) (eq) as suggested by Chantrell *et al.*<sup>67</sup>

592

$$M(\alpha) = M_s \int_0^\infty n_v(D_m) L(\alpha) dD_m \quad (2)$$

$$L(\alpha) = \coth \alpha - \frac{1}{\alpha}; \alpha = \frac{\pi \mu_0 M_d D_m^3 H}{6 k_B T} \quad (3)$$

$$n_v(D_m) = \frac{1}{\sqrt{2\pi} D_m \ln \sigma_m} \exp\left[-\frac{\ln^2(D_m / D_{mv})}{2 \ln^2 \sigma}\right] \quad (4)$$

593 where  $\alpha$  is the Langevin parameter,  $M_s$  is the saturation magnetization,  $D_{mv}$  is the volume-weighted  
 594 median magnetic diameter,  $\ln \sigma_m$  is the geometric deviation of the magnetic diameter distribution,  
 595  $\mu_0$  is the permeability of free space,  $k_B$  is Boltzmann's constant,  $M_d$  is the domain magnetization,  
 596 and  $T$  is the absolute temperature. The fitting of the magnetization curves to these equations using  
 597 a nonlinear regression model in MATLAB provided an estimate of the average magnetic  
 598 diameters, under the assumption that the magnetic domains are spherical. The saturation



599 magnetization ( $M_s$ ) was obtained from the maximum of the MH curve, normalized by mass of  
600 iron.

### 601 **X-ray diffraction**

602 A Rigaku MiniFlex600 X-ray diffractometer (40 kV, 15 mA) equipped with a D/teX Ultra2  
603 detector was used to characterize the crystal structure of iron oxide nanoparticles. For sample  
604 preparation, 300  $\mu$ L of purified nanoparticles in hexane were drop casted into a zero-background  
605 holder and scanned from 10 to 70  $^{\circ}$  at a step width of 0.005  $^{\circ}$  and scan speed of 0.10  $^{\circ}$ /min. The  
606 SmartLab Studio II software was used for analysis, starting with peak evaluation, fitting them to  
607 the split pseudo-Voigt function, and performing background refinement using the B-spline type.  
608 Estimates of crystal size used the Scherrer equation and peak broadening of the main peaks were  
609 averaged (30, 35, 53, and 56  $^{\circ}$ ).

### 610 **MPI performance**

611 MPI performance of nD-PEG coated nanoparticles in deionized water was first characterized by  
612 acquiring MPI RELAX<sup>TM</sup> scans (45 kHz, 16 mT in x-axis) of 5-15  $\mu$ L (1-2 mg/mL) in 200  $\mu$ L  
613 microcentrifuge tubes using the MOMENTUM<sup>TM</sup> scanner (Magnetic Insight, CA, USA). Each  
614 sample was placed in custom 3D-printed sample holder, centered in the MPI field of view (FOV),  
615 and scanned for 3-5 min. The signal of the x-space point spread function (PSF) obtained was  
616 normalized by iron mass for comparison. The MPI signal corresponds to the peak specific intensity  
617 reported in unit of  $\text{mg}_{\text{Fe}}^{-1}$ , and the resolution corresponds to the FWHM system-reported value in  
618 units of mT.

619 A dilution series of each of the nanoparticles synthesized using the Fe (II), Fe (III), and 1:2 Mix  
620 oleates were prepared for iron masses from 1000  $\text{ng}_{\text{Fe}}$  to 25  $\text{ng}_{\text{Fe}}$  for a 5  $\mu$ L sample volume.  
621 Triplicates were included for each sample by placing 3 capillary tubes (0.8 mm ID) with 5  $\mu$ L each  
622 perpendicular to the FOV. MPI scans were acquired with the MOMENTUM<sup>TM</sup> scanner (Magnetic  
623 Insight, CA, USA) using standard multichannel mode (45 kHz for x/z axes, 5.7 T/m). The images  
624 obtained through an x-space direct reconstruction, which applies an equalization filter,<sup>68, 69</sup> were  
625 analyzed using MATLAB (Mathworks, MA, USA) in-house algorithms in which the region of  
626 interest (ROI) was selected to obtain the maximum signal of each sample. The limit of detection  
627 is based on comparison to the signal obtained for a water sample, indicating the background signal



628 of nonmagnetic material, to make sure that the signal obtained from dilute samples is from the  
629 nanoparticles and not background signal fluctuations.

630 To evaluate imaging resolution of each sample, 2 capillary tubes (0.8 mm ID) with 5  $\mu$ L (5-10  $\mu$ g)  
631 each were placed parallel to the FOV separated by varying distances from the center of the samples  
632 (3.5-5 mm) and scanned with the MOMENTUM<sup>TM</sup> scanner (Magnetic Insight, CA, USA) in 2D  
633 standard mode with an x-space direct reconstruction (45 kHz for x/z axes, 5.7 T/m). The separation  
634 between the samples was decreased until the signal could not be separated, using the criteria that  
635 signals are separated when it is less than half the maximum signal in between the two capillaries.  
636 Finally, line scan profiles were obtained for the section with the maximum signal for the image,  
637 and these were normalized by the maximum signal to facilitate comparisons.

638 **Mössbauer Spectroscopy**

639 Mössbauer Spectroscopy measurements were performed with a <sup>57</sup>Co source, a Janis SHI-850-5  
640 cryogen-free cryostat, and Lakeshore 325 Temperature Controller. Hyperfine interaction  
641 parameters were analyzed using a least-squared fitting model with Mössbauer GenFit Software (R.  
642 S. Preston and D. E. Brown). Powdered samples were stored in an Argon atmosphere glovebox  
643 and were loaded and sealed into Mössbauer cups for characterization at 293K and 6K. Additional  
644 analysis details are provided in the Supporting Information.

645



646 **Conflicts of Interest**

647 CRR is an inventor on patents and patent applications, which are awarded or submitted in whole  
648 or in part to the University of Florida and are related to magnetic nanoparticles or magnetic particle  
649 imaging. The university may benefit financially from their commercialization, and the author  
650 could benefit under the university's patent policy. All other authors declare that they have no other  
651 competing interests.

652 **Data Availability**

653 The authors confirm that the data supporting the findings of this study are available within the  
654 article and its ESI. The raw datasets generated supporting the current study are available from the  
655 corresponding author on reasonable request.

656 **Acknowledgements**

657 This work was partly conducted at the Nanoscale Research Facility of the Herbert Wertheim  
658 College of Engineering at the University of Florida. Thank you to Dr. D. J. Milliron and Ph.D.  
659 student A. Singh at the University of Texas at Austin for allowing A. C. Velazquez-Albino to visit  
660 their laboratory and learn their methods for the esterification synthesis. We are grateful to D. P.  
661 Valdes for reviewing the manuscript.

662 **Funding Sources**

663 This manuscript is the result of funding by the National Institutes of Health (NIH) through the  
664 National Institute for Biomedical Imaging and Bioengineering (NIBIB) under award number  
665 R01EB031224, the National Cancer Institute (NCI) under award R21CA263653, and the National  
666 Institute of Neurological Disorders and Stroke (NINDS) under award R21NS125089. It is subject  
667 to the NIH Public Access Policy. Through acceptance of this federal funding, NIH has been given  
668 a right to make this manuscript publicly available in PubMed Central upon the Official Date of  
669 Publication, as defined by NIH.”

670 **Supporting Information**

671 Scheme of experimental set-up; additional representative TEM images of all samples; results of  
672 longer synthesis at 350 °C; results of flow rate experiment at 350 °C; FTIR spectra of Fe (II) and



673 Fe (III) oleates; full MH curves; tabulated Mössbauer spectroscopy hyperfine fitting parameters  
674 measured at 293 K and 6 K.

## 675 **Author Information**

676 \*Corresponding Author: Carlos M. Rinaldi-Ramos ([carlos.rinaldi@ufl.edu](mailto:carlos.rinaldi@ufl.edu))

## 677 **Author Contributions**

678 A.C.V.A. and C.M.R.R. conceptualized and designed the experiments. A.C.V.A. and B.E.  
679 performed nanoparticle synthesis and purification experiments. E.D.I. performed the Fe (III) oleate  
680 synthesis. A.C.V.A. performed TEM, SQUID, and XRD characterization of nanoparticles. N.E.  
681 performed polymer synthesis and coating of nanoparticles. A.W. performed Mössbauer  
682 spectroscopy experiments under J.A.J. supervision. C.E.J. and W.G. performed fitting and  
683 interpretation of Mössbauer spectra. A.M. and A.C.V.A. performed MPI experiments.

684 A.C.V.A. analyzed FTIR and SQUID data, meanwhile B.E. assisted her with TEM analysis.  
685 A.C.V.A. and M.M.B. analyzed XRD data. A.M., A.C.V.A., and C.M.R.R. analyzed MPI data.  
686 A.C.V.A. and C.M.R.R. contributed equally to visualization of the data. A.C.V.A. wrote the  
687 original draft, with main review and editing from C.M.R.R., and review of all co-authors. The  
688 manuscript was written through contributions of all authors. All authors have given approval to  
689 the final version of the manuscript.

## 690 **Abbreviations**

691 MPI – magnetic particle imaging; FTIR – Fourier transform infrared; nD-PEG – nitroDOPA-  
692 polyethylene glycol; DLS – dynamic light scattering; THF – tetrahydrofuran; MPMS-3 – magnetic  
693 property measurement system; SQUID – superconducting quantum interference device; FOV –  
694 field of view; PSF – point spread function; ROI – region of interest;  $D_p$  – physical diameter;  $\ln \sigma_p$   
695 – geometric deviation of physical diameter;  $\Delta v$  – separation of FTIR bands;  $D_m$  – magnetic  
696 diameter;  $\ln \sigma_m$  – geometric deviation of magnetic diameter; XRD – x-ray diffraction; FWHM –  
697 full width half-maximum; 2D – two-dimensional  
698

## 699 **References**

700 1. Gleich, B.; Weizenecker, J., Tomographic imaging using the nonlinear response of  
701 magnetic particles. *Nature* **2005**, *435* (7046), 1214-1217.

Open Access Article. Published on 08 January 2026. Downloaded on 1/10/2026 9:58:11 AM.  
This article is licensed under a Creative Commons Attribution-NonCommercial 3.0 Unported Licence.

(cc) BY-NC

702 2. Rivera-Rodriguez, A.; Hoang-Minh, L. B.; Chiu-Lam, A.; Sarna, N.; Marrero-Morales, L.;  
703 Mitchell, D. A.; Rinaldi-Ramos, C. M., Tracking adoptive T cell immunotherapy using magnetic  
704 particle imaging. *Nanotheranostics* **2021**, *5* (4), 431-444.

705 3. Rivera-Rodriguez, A.; Rinaldi-Ramos, C. M., Emerging Biomedical Applications Based  
706 on the Response of Magnetic Nanoparticles to Time-Varying Magnetic Fields. *Annual Review of  
707 Chemical and Biomolecular Engineering* **2021**, *12* (1), 163-185.

708 4. Liu, S.; Chiu-Lam, A.; Rivera-Rodriguez, A.; DeGroff, R.; Savliwala, S.; Sarna, N.;  
709 Rinaldi-Ramos, C. M., Long circulating tracer tailored for magnetic particle imaging.  
710 *Nanotheranostics* **2021**, *5* (3), 348-361.

711 5. Song, G.; Chen, M.; Zhang, Y.; Cui, L.; Qu, H.; Zheng, X.; Wintermark, M.; Liu, Z.; Rao,  
712 J., Janus Iron Oxides @ Semiconducting Polymer Nanoparticle Tracer for Cell Tracking by  
713 Magnetic Particle Imaging. *Nano Letters* **2018**, *18* (1), 182-189.

714 6. Wang, Q.; Ma, X.; Liao, H.; Liang, Z.; Li, F.; Tian, J.; Ling, D., Artificially Engineered  
715 Cubic Iron Oxide Nanoparticle as a High-Performance Magnetic Particle Imaging Tracer for Stem  
716 Cell Tracking. *ACS Nano* **2020**, *14* (2), 2053-2062.

717 7. Sehl, O. C.; Foster, P. J., The sensitivity of magnetic particle imaging and fluorine-19  
718 magnetic resonance imaging for cell tracking. *Sci Rep* **2021**, *11* (1), 22198.

719 8. Julia J. Gevaert, K. V. B., Olivia C. Sehl, Paula J. Foster, VivoTrax+ improves the detection  
720 of cancer cells with magnetic particle imaging. *International Journal on Magnetic Particle  
721 Imaging IJMPI* **2022**, Vol 8.

722 9. Antonelli, A.; Szwargulski, P.; Scarpa, E.-S.; Thieben, F.; Cordula, G.; Ambrosi, G.; Guidi,  
723 L.; Ludewig, P.; Knopp, T.; Magnani, M., Development of long circulating magnetic particle  
724 imaging tracers: use of novel magnetic nanoparticles and entrapment into human erythrocytes.  
725 *Nanomedicine* **2020**, *15* (8), 739-753.

726 10. Rahmer, J.; Antonelli, A.; Sfara, C.; Tiemann, B.; Gleich, B.; Magnani, M.; Weizenecker,  
727 J.; Borgert, J., Nanoparticle encapsulation in red blood cells enables blood-pool magnetic particle  
728 imaging hours after injection. *Physics in Medicine and Biology* **2013**, *58* (12), 3965-3977.

729 11. Khandhar, A. P.; Keselman, P.; Kemp, S. J.; Ferguson, R. M.; Goodwill, P. W.; Conolly,  
730 S. M.; Krishnan, K. M., Evaluation of PEG-coated iron oxide nanoparticles as blood pool tracers  
731 for preclinical magnetic particle imaging. *Nanoscale* **2017**, *9* (3), 1299-1306.

732 12. Kratz, H.; Mohtasham Dolatshahi, A.; Eberbeck, D.; Kosch, O.; Wiekhorst, F.; Taupitz, M.;  
733 Hamm, B.; Stolzenburg, N.; Schnorr, J., Tailored Magnetic Multicore Nanoparticles for Use as  
734 Blood Pool MPI Tracers. *Nanomaterials* **2021**, *11* (6), 1532.

735 13. Orendorff, R.; Peck, A. J.; Zheng, B.; Shirazi, S. N.; Ferguson, R. M.; Khandhar, A. P.;  
736 Kemp, S. J.; Goodwill, P.; Krishnan, K. M.; Brooks, G. A.; Kaufer, D.; Conolly, S., Firstin  
737 vivotraumatic brain injury imaging via magnetic particle imaging. *Physics in Medicine and  
738 Biology* **2017**, *62* (9), 3501-3509.

739 14. Bulte, J. W. M.; Walczak, P.; Janowski, M.; Krishnan, K. M.; Arami, H.; Halkola, A.;  
740 Gleich, B.; Rahmer, J., Quantitative “Hot-Spot” Imaging of Transplanted Stem Cells Using  
741 Superparamagnetic Tracers and Magnetic Particle Imaging. *Tomography* **2015**, *1* (2), 91-97.

742 15. Lechermann, L. M.; Lau, D.; Attili, B.; Aloj, L.; Gallagher, F. A., In Vivo Cell Tracking  
743 Using PET: Opportunities and Challenges for Clinical Translation in Oncology. *Cancers* **2021**, *13*  
744 (16), 4042.

745 16. Goodwill, P. W.; Conolly, S. M., The X-Space Formulation of the Magnetic Particle  
746 Imaging Process: 1-D Signal, Resolution, Bandwidth, SNR, SAR, and Magnetostimulation. *IEEE  
747 Transactions on Medical Imaging* **2010**, *29* (11), 1851-1859.

748 17. Velazquez-Albino, A. C.; Imhoff, E. D.; Rinaldi-Ramos, C. M., Advances in engineering  
749 nanoparticles for magnetic particle imaging (MPI). *Science Advances* **2025**, *11* (2), eado7356.  
750 18. Velazquez-Albino, A. C.; Nozka, A.; Melnyk, A.; Good, H. J.; Rinaldi-Ramos, C. M., Post-  
751 synthesis Oxidation of Superparamagnetic Iron Oxide Nanoparticles to Enhance Magnetic Particle  
752 Imaging Performance. *ACS Applied Nano Materials* **2023**, *7* (1), 279-291.  
753 19. Graeser, M.; Knopp, T.; Szwargulski, P.; Friedrich, T.; von Gladiss, A.; Kaul, M.;  
754 Krishnan, K. M.; Ittrich, H.; Adam, G.; Buzug, T. M. Towards Picogram Detection of  
755 Superparamagnetic Iron-Oxide Particles Using a Gradiometric Receive Coil *Sci Rep* [Online],  
756 2017, p. 6872. PubMed. <http://europepmc.org/abstract/MED/28761103>  
757 <https://doi.org/10.1038/s41598-017-06992-5>  
758 <https://europepmc.org/articles/PMC5537232>  
759 <https://europepmc.org/articles/PMC5537232?pdf=render>  
760 <https://www.nature.com/articles/s41598-017-06992-5.pdf> (accessed 2017/07//).  
761 20. Keselman, P.; Yu, E. Y.; Zhou, X. Y.; Goodwill, P. W.; Chandrasekharan, P.; Ferguson,  
762 R. M.; Khandhar, A. P.; Kemp, S. J.; Krishnan, K. M.; Zheng, B.; Conolly, S. M., Tracking short-  
763 term biodistribution and long-term clearance of SPIO tracers in magnetic particle imaging. *Physics*  
764 *in Medicine and Biology* **2017**, *62* (9), 3440-3453.  
765 21. Ludewig, P.; Gdaniec, N.; Sedlacik, J.; Forkert, N. D.; Szwargulski, P.; Graeser, M.; Adam,  
766 G.; Kaul, M. G.; Krishnan, K. M.; Ferguson, R. M.; Khandhar, A. P.; Walczak, P.; Fiehler, J.;  
767 Thomalla, G.; Gerloff, C.; Knopp, T.; Magnus, T., Magnetic Particle Imaging for Real-Time  
768 Perfusion Imaging in Acute Stroke. *ACS Nano* **2017**, *11* (10), 10480-10488.  
769 22. Kaul, M. G.; Mummert, T.; Jung, C.; Salamon, J.; Khandhar, A. P.; Ferguson, R. M.;  
770 Kemp, S. J.; Ittrich, H.; Krishnan, K. M.; Adam, G.; Knopp, T., In vitro and in vivo comparison  
771 of a tailored magnetic particle imaging blood pool tracer with Resovist. *Physics in Medicine and*  
772 *Biology* **2017**, *62* (9), 3454-3469.  
773 23. Yu, E. Y.; Chandrasekharan, P.; Berzon, R.; Tay, Z. W.; Zhou, X. Y.; Khandhar, A. P.;  
774 Ferguson, R. M.; Kemp, S. J.; Zheng, B.; Goodwill, P. W.; Wendland, M. F.; Krishnan, K. M.;  
775 Behr, S.; Carter, J.; Conolly, S. M., Magnetic Particle Imaging for Highly Sensitive, Quantitative,  
776 and Safe *< i>in Vivo</i>* Gut Bleed Detection in a Murine Model. *ACS Nano* **2017**, *11* (12), 12067-  
777 12076.  
778 24. Yu, E. Y.; Bishop, M.; Zheng, B.; Ferguson, R. M.; Khandhar, A. P.; Kemp, S. J.; Krishnan,  
779 K. M.; Goodwill, P. W.; Conolly, S. M., Magnetic Particle Imaging: A Novel *in Vivo* Imaging  
780 Platform for Cancer Detection. *Nano Letters* **2017**, *17* (3), 1648-1654.  
781 25. Ferguson, R. M.; Khandhar, A. P.; Kemp, S. J.; Arami, H.; Saritas, E. U.; Croft, L. R.;  
782 Konkle, J.; Goodwill, P. W.; Halkola, A.; Rahmer, J.; Borgert, J.; Conolly, S. M.; Krishnan, K.  
783 M., Magnetic Particle Imaging With Tailored Iron Oxide Nanoparticle Tracers. *IEEE Transactions*  
784 *on Medical Imaging* **2015**, *34* (5), 1077-1084.  
785 26. Park, J.; An, K.; Hwang, Y.; Park, J.-G.; Noh, H.-J.; Kim, J.-Y.; Park, J.-H.; Hwang, N.-  
786 M.; Hyeon, T., Ultra-large-scale syntheses of monodisperse nanocrystals. *Nature Mater* **2004**, *3*  
787 (12), 891-895.  
788 27. Gevart, T.; Freis, B.; Vangijzegem, T.; Ramirez, M. L. A.; Stanicki, D.; Begin, S.; Laurent,  
789 S., Design of Iron Oxide Nanoparticles as Theranostic Nanoplatforms for Cancer Treatment. In  
790 *Topics in Applied Physics*, Springer International Publishing: 2024; pp 175-215.  
791 28. Kemp, S. J.; Ferguson, R. M.; Khandhar, A. P.; Krishnan, K. M., Monodisperse magnetite  
792 nanoparticles with nearly ideal saturation magnetization. *RSC Adv.* **2016**, *6* (81), 77452-77464.



Open Access Article. Published on 08 January 2026. Downloaded on 1/10/2026 9:58:11 AM.  
This article is licensed under a Creative Commons Attribution-NonCommercial 3.0 Unported Licence.

793 29. Unni, M.; Uhl, A. M.; Savliwala, S.; Savitzky, B. H.; Dhavalikar, R.; Garraud, N.; Arnold,  
794 D. P.; Kourkoutis, L. F.; Andrew, J. S.; Rinaldi, C., Thermal Decomposition Synthesis of Iron  
795 Oxide Nanoparticles with Diminished Magnetic Dead Layer by Controlled Addition of Oxygen.  
796 *ACS Nano* **2017**, *11* (2), 2284-2303.

797 30. Chen, R.; Christiansen, M. G.; Sourakov, A.; Mohr, A.; Matsumoto, Y.; Okada, S.;  
798 Jasanoff, A.; Anikeeva, P., High-Performance Ferrite Nanoparticles through Nonaqueous Redox  
799 Phase Tuning. *Nano Letters* **2016**, *16* (2), 1345-1351.

800 31. Liz-Marzán, L. M.; Kagan, C. R.; Millstone, J. E., Reproducibility in Nanocrystal  
801 Synthesis? Watch Out for Impurities! *ACS Nano* **2020**, *14* (6), 6359-6361.

802 32. Khan, Z.; Javed, F.; Shamair, Z.; Hafeez, A.; Fazal, T.; Aslam, A.; Zimmerman, W. B.;  
803 Rehman, F., Current developments in esterification reaction: A review on process and parameters.  
804 *Journal of Industrial and Engineering Chemistry* **2021**, *103*, 80-101.

805 33. Singhal, A.; Achary, S. N.; Manjanna, J.; Chatterjee, S.; Ayyub, P.; Tyagi, A. K., Chemical  
806 Synthesis and Structural and Magnetic Properties of Dispersible Cobalt- and Nickel-Doped ZnO  
807 Nanocrystals. *The Journal of Physical Chemistry C* **2010**, *114* (8), 3422-3430.

808 34. Ito, D.; Yokoyama, S.; Zaikova, T.; Masuko, K.; Hutchison, J. E., Synthesis of Ligand-  
809 Stabilized Metal Oxide Nanocrystals and Epitaxial Core/Shell Nanocrystals <i>via</i> a Lower-  
810 Temperature Esterification Process. *ACS Nano* **2014**, *8* (1), 64-75.

811 35. Vreeland, E. C.; Watt, J.; Schober, G. B.; Hance, B. G.; Austin, M. J.; Price, A. D.; Fellows,  
812 B. D.; Monson, T. C.; Hudak, N. S.; Maldonado-Camargo, L.; Bohorquez, A. C.; Rinaldi, C.;  
813 Huber, D. L., Enhanced Nanoparticle Size Control by Extending LaMer's Mechanism. *Chem.  
814 Mater.* **2015**, *27* (17), 6059-6066.

815 36. Jansons, A. W.; Hutchison, J. E., Continuous Growth of Metal Oxide Nanocrystals: Enhanced  
816 Control of Nanocrystal Size and Radial Dopant Distribution. *ACS Nano* **2016**, *10* (7),  
817 6942-6951.

818 37. Jansons, A. W.; Koskela, K. M.; Crockett, B. M.; Hutchison, J. E., Transition Metal-Doped  
819 Metal Oxide Nanocrystals: Efficient Substitutional Doping through a Continuous Growth Process.  
820 *Chem. Mater.* **2017**, *29* (19), 8167-8176.

821 38. Cooper, S. R.; Candler, R. O.; Cosby, A. G.; Johnson, D. W.; Jensen, K. M. Ø.; Hutchison,  
822 J. E., Evolution of Atomic-Level Structure in Sub-10 Nanometer Iron Oxide Nanocrystals:  
823 Influence on Cation Occupancy and Growth Rates. *ACS Nano* **2020**, *14* (5), 5480-5490.

824 39. Cooper, S. R.; Plummer, L. K.; Cosby, A. G.; Lenox, P.; Jander, A.; Dhagat, P.; Hutchison,  
825 J. E., Insights into the Magnetic Properties of Sub-10 nm Iron Oxide Nanocrystals through the Use  
826 of a Continuous Growth Synthesis. *Chem. Mater.* **2018**, *30* (17), 6053-6062.

827 40. Plummer, L. K.; Crockett, B. M.; Pennel, M. L.; Jansons, A. W.; Koskela, K. M.;  
828 Hutchison, J. E., Influence of Monomer Flux and Temperature on Morphology of Indium Oxide  
829 Nanocrystals during a Continuous Growth Synthesis. *Chem. Mater.* **2019**, *31* (18), 7638-7649.

830 41. Plummer, L. K.; Hutchison, J. E., Understanding the Effects of Iron Precursor Ligation and  
831 Oxidation State Leads to Improved Synthetic Control for Spinel Iron Oxide Nanocrystals.  
832 *Inorganic Chemistry* **2020**, *59* (20), 15074-15087.

833 42. Kim, K.; Yu, J.; Noh, J.; Reimnitz, L. C.; Chang, M.; Gamelin, D. R.; Korgel, B. A.;  
834 Hwang, G. S.; Milliron, D. J., Synthetic Control of Intrinsic Defect Formation in Metal Oxide  
835 Nanocrystals Using Dissociated Spectator Metal Salts. *Journal of the American Chemical Society*  
836 **2022**, *144* (50), 22941-22949.



837 43. Milliron, K. K. L. C. R. S. H. C. J. N. Z. D. S. L. G. B. A. K. D. J., Effect of  
838 Nonincorporative Cations on the Size and Shape of Indium Oxide Nanocrystals. *Chem. Mater.*  
839 **2020**.

840 44. Hutchison, T. A. K. a. J. E., Precursor and Surface Reactivities Influence the Early Growth  
841 of Indium Oxide Nanocrystals in a Reagent-Driven, Continuous Addition Synthesis. *Chem. Mater.*  
842 **2023**, *35* (8), 3151-3161.

843 45. Jansons, A. W.; Plummer, L. K.; Hutchison, J. E., Living Nanocrystals. *Chem. Mater.*  
844 **2017**, *29* (13), 5415-5425.

845 46. Bronstein, L. M.; Huang, X.; Retrum, J.; Schmucker, A.; Pink, M.; Stein, B. D.; Dragnea,  
846 B., Influence of Iron Oleate Complex Structure on Iron Oxide Nanoparticle Formation. *Chem.*  
847 *Mater.* **2007**, *19* (15), 3624-3632.

848 47. Cotin, G.; Kiefer, C.; Perton, F.; Ihiawakrim, D.; Blanco-Andujar, C.; Moldovan, S.;  
849 Lefevre, C.; Ersen, O.; Pichon, B.; Mertz, D.; Bégin-Colin, S., Unravelling the Thermal  
850 Decomposition Parameters for The Synthesis of Anisotropic Iron Oxide Nanoparticles.  
851 *Nanomaterials* **2018**, *8* (11), 881.

852 48. Nader, K.; Castellanos-Rubio, I.; Orue, I.; Iglesias-Rojas, D.; Barón, A.; Gil de Muro, I.;  
853 Lezama, L.; Insausti, M., Getting insight into how iron(III) oleate precursors affect the features of  
854 magnetite nanoparticles. *Journal of Solid State Chemistry* **2022**, *316*, 123619.

855 49. Park, S.-J.; Kim, S.; Lee, S.; Khim, Z. G.; Char, K.; Hyeon, T., Synthesis and Magnetic  
856 Studies of Uniform Iron Nanorods and Nanospheres. *Journal of the American Chemical Society*  
857 **2000**, *122* (35), 8581-8582.

858 50. Sun, S.; Murray, C. B.; Weller, D.; Folks, L.; Moser, A., Monodisperse FePt Nanoparticles  
859 and Ferromagnetic FePt Nanocrystal Superlattices. *Science* **2000**, *287* (5460), 1989-1992.

860 51. Sun, S.; Zeng, H.; Robinson, D. B.; Raoux, S.; Rice, P. M.; Wang, S. X.; Li, G.,  
861 Monodisperse MFe<sub>2</sub>O<sub>4</sub> (M = Fe, Co, Mn) Nanoparticles. *Journal of the American Chemical Society*  
862 **2004**, *126* (1), 273-279.

863 52. Sun, S.; Zeng, H., Size-Controlled Synthesis of Magnetite Nanoparticles. *Journal of the*  
864 *American Chemical Society* **2002**, *124* (28), 8204-8205.

865 53. Hyeon, T.; Lee, S. S.; Park, J.; Chung, Y.; Na, H. B., Synthesis of Highly Crystalline and  
866 Monodisperse Maghemite Nanocrystallites without a Size-Selection Process. *Journal of the*  
867 *American Chemical Society* **2001**, *123* (51), 12798-12801.

868 54. Claramonte, M. D. C.; Vilchez, F. G.; Vialard, A. P., Thermal behaviour and heat capacity  
869 of some high molecular weight alcohols and esters used in pharmaceutical preparations.  
870 *Thermochimica Acta* **1993**, *222* (2), 209-218.

871 55. Hufschmid, R.; Arami, H.; Ferguson, R. M.; Gonzales, M.; Teeman, E.; Brush, L. N.;  
872 Browning, N. D.; Krishnan, K. M., Synthesis of phase-pure and monodisperse iron oxide  
873 nanoparticles by thermal decomposition. *Nanoscale* **2015**, *7* (25), 11142-11154.

874 56. Llacer-Wintle, J.; Hertle, L.; Ziegler, S.; Pellicer, E.; Roca, A. G.; Nogués, J.;  
875 Puigmartí-Luis, J.; Nelson, B. J.; Chen, X. Z.; Pané, S., A Simple In Situ Marker Guiding  
876 Shape-Controlled Synthesis of Iron Oxide Nanoparticles. *Advanced Functional Materials* **2024**.

877 57. Hyeon, T., Chemical synthesis of magnetic nanoparticles. *Chemical Communications*  
878 **2003**, (8), 927-934.

879 58. Pichon, B. P.; Gerber, O.; Lefevre, C.; Florea, I.; Fleutot, S.; Baaziz, W.; Pauly, M.;  
880 Ohlmann, M.; Ulhaq, C.; Ersen, O.; Pierron-Bohnes, V.; Panissod, P.; Drillon, M.; Begin-Colin,  
881 S., Microstructural and Magnetic Investigations of Wüstite-Spinel Core-Shell Cubic-Shaped  
882 Nanoparticles. *Chem. Mater.* **2011**, *23* (11), 2886-2900.



Open Access Article. Published on 08 January 2026. Downloaded on 1/10/2026 9:58:11 AM.  
This article is licensed under a Creative Commons Attribution-NonCommercial 3.0 Unported Licence.  


883 59. Casula, M. F.; Jun, Y.-w.; Zaziski, D. J.; Chan, E. M.; Corrias, A.; Alivisatos, A. P., The  
884 Concept of Delayed Nucleation in Nanocrystal Growth Demonstrated for the Case of Iron Oxide  
885 Nanodisks. *Journal of the American Chemical Society* **2006**, *128* (5), 1675-1682.  
886 60. Chalasani, R.; Vasudevan, S., Form, Content, and Magnetism in Iron Oxide Nanocrystals.  
887 *The Journal of Physical Chemistry C* **2011**, *115* (37), 18088-18093.  
888 61. Orozco-Henao, J. M.; Alí, F. L.; Azcárate, J. C.; Robledo Candia, L. D.; Pasquevich, G.;  
889 Mendoza Zélis, P.; Haas, B.; Coogan, K.; Kirmse, H.; Koch, C. T.; Vericat, C.; Lavorato, G. C.;  
890 Fonticelli, M. H., Oxidation Kinetics of Magnetite Nanoparticles: Blocking Effect of Surface  
891 Ligands and Implications for the Design of Magnetic Nanoheaters. *Chem. Mater.* **2024**, *36* (22),  
892 11095-11108.  
893 62. Imhoff, E. D.; Melnyk, A.; Rinaldi-Ramos, C. M., Characterization and evaluation of  
894 commercial tracers for x-space magnetic particle imaging. *Journal of Magnetism and Magnetic*  
895 *Materials* **2025**, *620*, 172889.  
896 63. Barrera, C.; Herrera, A. P.; Rinaldi, C., Colloidal dispersions of monodisperse magnetite  
897 nanoparticles modified with poly(ethylene glycol). *J Colloid Interface Sci* **2009**, *329* (1), 107-13.  
898 64. Barrera, C.; Herrera, A. P.; Bezares, N.; Fachini, E.; Olayo-Valles, R.; Hinestrosa, J. P.;  
899 Rinaldi, C., Effect of poly(ethylene oxide)-silane graft molecular weight on the colloidal properties  
900 of iron oxide nanoparticles for biomedical applications. *J Colloid Interface Sci* **2012**, *377* (1), 40-  
901 50.  
902 65. Chiu-Lam, A.; Staples, E.; Pepine, C. J.; Rinaldi, C., Perfusion, cryopreservation, and  
903 nanowarming of whole hearts using colloidally stable magnetic cryopreservation agent solutions.  
904 *Science Advances* **2021**, *7* (2), eabe3005.  
905 66. De Palma, R.; Peeters, S.; Van Bael, M. J.; Van den Rul, H.; Bonroy, K.; Laureyn, W.;  
906 Mullens, J.; Borghs, G.; Maes, G., Silane Ligand Exchange to Make Hydrophobic  
907 Superparamagnetic Nanoparticles Water-Dispersible. *Chem. Mater.* **2007**, *19* (7), 1821-1831.  
908 67. Chantrell, R.; Popplewell, J.; Charles, S., Measurements of particle size distribution  
909 parameters in ferrofluids. *IEEE Transactions on Magnetics* **1978**, *14* (5), 975-977.  
910 68. Lu, K.; Goodwill, P.; Zheng, B.; Conolly, S., Multi-Channel Acquisition for Isotropic  
911 Resolution in Magnetic Particle Imaging. *IEEE Transactions on Medical Imaging* **2018**, *37* (9),  
912 1989-1998.  
913 69. Lu, K.; Goodwill, P.; Zheng, B.; Conolly, S. In *Reshaping the 2D MPI PSF to be isotropic*  
914 *and sharp using vector acquisition and equalization*, 2015 5th International Workshop on  
915 Magnetic Particle Imaging (IWMPI), 2015-03-01; IEEE: 2015; pp 1-1.  
916

## Data Availability

The authors confirm that the data supporting the findings of this study are available within the article and its ESI. The raw datasets generated supporting the current study are available from the corresponding author on reasonable request.

